1 # Remote sensing of young leaf photosynthetic capacity in tropical and subtropical

2 ## evergreen broadleaved forests

3   Xueqin Yang[1, 2, 6,#], Qingling Sun[2,#], Liusheng Han[3], Wenping Yuan[4], Jie Tian[2], Liyang Liu[5], Wei Zheng[2], Mei

4   Wang[2], Yunpeng Wang[1,6], Xiuzhi Chen[2,*]

5   [1] Guangzhou Institute of Geochemistry, Chinese Academy of Sciences, Guangzhou 510640, China

6   [2] Guangdong Province Data Center of Terrestrial and Marine Ecosystems Carbon Cycle, School of Atmospheric

7   Sciences, Sun Yat-sen University, Zhuhai 519082, China;

8   [3] School of Civil Engineering and Geomatics, Shandong University of Technology, Zibo 255000, China;

9   [4] College of Urban and Environmental Sciences, School of Urban Planning and Design, Peking University, Beijing

10   100871, China;

11   [5] Laboratoire des Sciences du Climat et de l'Environnement, IPSL, CEA-CNRS-UVSQ, Université Paris-Saclay,

12   91191 Gif sur Yvette, France;

13   [6] College of Earth and Planetary Sciences, University of Chinese Academy of Sciences, Beijing 101408, China;

14   [#] These authors contributed equally;

15   [*] *Correspondance: Xiuzhi Chen (chenxzh73@mail.sysu.edu.cn)*

17 **Abstract**

18   Determining the large-scale Rubisco carboxylation maximum rate ($V_{c,max25}$) in relation to leaf age is

19   crucial for assessing the photosynthetic capacity of canopy leaves in global forests. Young leaves (≤180 days)

20   with higher $V_{c,max25}$ compared with old leaves (>180 days) largely control the seasonality of leaf

21   photosynthetic capacity in tropical and subtropical evergreen broadleaved forests (TEFs). Nevertheless, it

22   has not yet been adequately quantified across TEFs. In this study, we propose an innovative method that

23   leverages neighborhood pixel analysis with a nonlinear least squares fitting approach to derive the $V_{c,max25}$ of

24   the young leaves at 0.25° spatial resolution from satellite-based solar-induced chlorophyll fluorescence (SIF)

25   products spanning from 2001 to 2018, which were reconstructed using both the TROPOMI (Tropospheric

26   Monitoring Instrument) SIF and MODIS reflectance data (RTSIF). Validations against in situ observations

27   show that the newly developed $V_{c,max25}$ products accurately capture the seasonality of the young leaf area in

28   South America and subtropical Asia, with correlation coefficients equal to 0.837, 0.661, and 0.952,

29   respectively. Additionally, the $V_{c,max25}$ of the young leaves simulated from the RTSIF is effectively correlated

30   (R>0.512) with that dissolved from the gridded gross primary production (GOSIF-derived GPP).

31   Furthermore, the gridded young leaf $V_{c,max25}$ dataset effectively detects the green-up region during the dry

32   seasons in the tropics, where the average annual precipitation exceeds 2000 mm/year. The clustering patterns

33   of the young leaf $V_{c,max25}$ also effectively match those clustered by climatic variables across the TEFs. Overall,

34   the newly developed $V_{c,max25}$ product is the first satellite-based dataset for addressing the $V_{c,max25}$ of

35   photosynthetically efficient young leaves and can provide useful information for modeling the large-scale

36   photosynthesis dynamics and thus carbon cycle across the TEFs. Herein, we provide the time series of $V_{c,max25}$

37   derived from RTSIF GPP as the main dataset and GOSIF- and FLUXCOM- derived as supplementary

38   datasets. These $V_{c,max25}$ products are available at https://doi.org/10.5281/zenodo.14807414 (Yang et al., 2025).

39

40 **Keywords:** maximum rate of carboxylation ($V_{c,max25}$), leaf age, photosynthesis, tropical and subtropical forest.

41

42 ## 1. Introduction

43 The maximum carboxylation rate ($V_{c,max}$) is the key leaf attribute that strongly influences the seasonal

44 variations in canopy photosynthesis in tropical and subtropical evergreen broadleaved forests (TEFs; Chen
45 et al., 2022; Wu et al., 2018). This is because $V_{c,max}$ is highly correlated with nitrogen-related plant functional
46 traits (Dechant et al., 2017; Lu et al., 2020), such as leaf nitrogen and chlorophyll content (Lu et al., 2020).
47 However, such nitrogen contents differ greatly at the large scale because the assignment of leaf nitrogen
48 varies in response to many other biotic and abiotic factors (Quebbeman and Ramirez, 2016), such as leaf
49 lifespan (Onoda et al., 2017), leaf temperature (Verheijen et al., 2013), light intensity (Hikosaka, 2014) and
50 species (Evans, 1989). While the large-scale leaf nitrogen is difficult to retrieve from remotely sensed data
51 (Knyazikhin et al., 2013), currently, mapping the regional or global scale $V_{c,max}$ is still challenging.

52     $V_{c,max}$ at 25°C (hereafter denoted as $V_{c,max25}$) is used as a benchmark in most ecosystem modeling for
53 simulating various $V_{c,max}$ values at different temperatures. For instance, the Farquhar-von Caemmerer-Berry
54 (FvCB) leaf photosynthetic model has been widely adopted for simulating plant photosynthesis across
55 different ecosystems (Farquhar et al., 1980; Sun et al., 2015), in which $V_{c,max25}$ is an essential parameter in
56 the FvCB model for determining leaf photosynthetic capacity. However, $V_{c,max25}$ also varies greatly across
57 different tree species and may even show a 2-3-fold difference across the same species (Orndahl et al., 2022).
58 Researches on this issue at the continental scale remain limited and inconclusive, mainly due to the diverse
59 seasonal constraints imposed by the water availability and light; these factors affect leaf scour and defoliation
60 across different climatic zones (Sulc et al., 2017; Kiehn et al., 2013). Recently, two independent satellite
61 remote sensing approaches have been developed with the objective of estimating $V_{c,max25}$ on a global scale.
62 The first satellite-based approach to deriving $V_{c,max25}$ is via leaf chlorophyll content (LCC) (Luo et al., 2019;
63 Lu et al., 2020). Chlorophyll harvests light and provides energy for reactions in the Calvin-Benson-Bassham
64 (CBB) cycle of photosynthesis (Luo et al., 2019). Thus, $V_{c,max25}$ is coordinated with LCC as plants optimize
65 their photosynthetic nitrogen resources (Croft et al., 2020; Xu et al., 2022a; 2022b). The retrieval of $V_{c,max25}$
66 from LCC offers the means of reliable and accurate $V_{c,max25}$ estimation over different spatiotemporal scales.
67 The second satellite-based approach is to deriving $V_{c,max25}$ is via solar-induced chlorophyll fluorescence (SIF)
68 (Mohammed et al., 2019). This is because SIF can serve as a good proxy for mapping gross primary
69 productivity (GPP) at the global scale (Frankenberg et al., 2011; Mohammed et al., 2019). To date, a time
70 series of daily $V_{c,max25}$ maps has been derived using SIF data obtained from the Global Ozone Monitoring
71 Experiment-2 (GOME-2) sensor, spanning the period from 2007 to 2017, with a resolution of 36 km (He et
72 al., 2019). However, there are both strengths and weaknesses of the $V_{c,max25}$ products derived from LCC and
73 SIF. LCCs have been reliably derived from multispectral satellite data at much higher resolution in space and
74 time than SIFs (Chen et al., 2022). Nevertheless, the derivation of LCC from remote sensing data is
75 susceptible to errors in the vegetation structural parameters employed in the derivation (Luo et al., 2019).
76 The conversion of LCC to $V_{c,max25}$ is contingent upon empirical relationships for disparate PFTs, which are
77 subject to considerable uncertainties (Chou et al., 2020; Croft et al., 2017; Houborg et al., 2013; 2015). In
78 contrast, SIF is directly related to vegetation photosynthetic rates, but the spatial and temporal resolution of
79 most satellite SIF observations is relatively low (Liu et al., 2024; Chen et al., 2022). One most recent study
80 demonstrated that TROPOMI SIF data with high spatial and temporal resolutions exhibit a linear relationship
81 with GPP, containing robust signals for $V_{c,max25}$ (Chen et al., 2022). Thus TROPOMI SIF data have been
82 extensively employed for simulating plant photosynthesis across diverse ecosystems (Yang et al., 2023).

83   TEFs constitute 40-50% of the carbon sinks in global forest ecosystems and thus play a central role in
84 the global carbon cycle (Yang et al., 2023; Lu et al., 2021). Despite the perennial nature of the TEFs canopy,
85 recent research indicates that photosynthesis in these forests exhibits significant seasonal fluctuations (Wu et
86 al., 2016). This seasonality in canopy photosynthesis across TEFs primarily stems from the seasonal
87 variability of canopy leaf age structures (Chen et al., 2021; 2022), which are mainly driven by climatic

88 seasonality (Li et al., 2021; Yang et al., 2021). Recent studies have demonstrated that young leaves (≤180
89 days) often show higher $V_{c,max25}$ compared with old leaves (>180 days) and thus largely control the seasonality
90 of leaf photosynthetic capacity in TEFs (Locke and Ort, 2014; Wu et al., 2016). Thus, mapping the $V_{c,max25}$
91 seasonality of young leaves becomes more important for modeling the tropical photosynthesis seasonality at
92 the continental scale. However, satellite-based studies still have challenges in accurately differentiating
93 $V_{c,max25}$ across the leaf age groups in TEFs due to the intricate mechanism of climate influences on the leaf
94 age in TEFs (Jensen et al., 2015; Song et al., 2020). This issue thus complicates the accurate depiction of
95 $V_{c,max25}$ seasonality related to young leaf age. While Earth system models (ESMs) frequently struggle to
96 precisely replicate the seasonal variations in $V_{c,max25}$ among the various leaf age categories (Atkin et al., 2014;
97 Ali et al., 2016). The most difficult issue still stems from the insufficiently understood mechanisms that
98 connect the seasonal changes in water and light availability to the patterns of leaf emergence and shedding.

99 To solve above-mentioned gaps in mapping the $V_{c,max25}$ of young leaves , here we categorized the canopy
100 foliage of TEFs into two distinct leaf age groups: young (<180 days) and old (>180 days) leaves. Then, we
101 proposed an innovative neighbor-based approach to determine the maximum carboxylation rate ($V_{c,max25}$) for
102 the young leaf cohort by setting a constant $V_{c,max25}$ for the old leaf cohort (Yang et al., 2023), as $V_{c,max25}$ of
103 the old leaf cohort varies very small (Chen et al.,2019; Albert et al., 2018). This research has three specific
104 objectives: (1) to create a global gridded dataset that maps the seasonal variability in young leaf $V_{c,max25}$ across
105 entire TEFs from 2001 to 2018; (2) to evaluate the accuracy of these datasets against ground-based
106 measurements and dissolved $V_{c,max25}$ data from the GOSIF-derived GPP datasets; and (3) to analyze the
107 seasonal fluctuations in the young leaf $V_{c,max25}$ across the entire TEFs. This newly developed $V_{c,max25}$ dataset
108 can help to provides new insights into tropical and subtropical phenology by detailing the seasonality of
109 young leave $V_{c,max25}$. This valuable information can also aid in the refinement and improvement of the tropical
110 phenological models used in the ESMs.

111

112 ## 2. Materials and methods
113 ### 2.1 Study area
114 The studied TEFs were identified by selecting pixels marked as EBF (Evergreen Broadleaf Forest; Sulla-
115 Menashe et al., 2018) on MODIS MCD12C1 land cover maps at 0.05° spatial resolution (see **Fig. 1**). TEFs
116 in South America are the largest tropical rainforests in the world and are mainly located at 18°N ~30°S and
117 40~90°W, followed by TEFs in tropical Africa (10°N~10°S, 10°W~30°E). TEFs in tropical Asia are mainly
118 located in the Malay Archipelago, Asian Peninsula and northern Australia (30°N~20°S, 70~150°E).
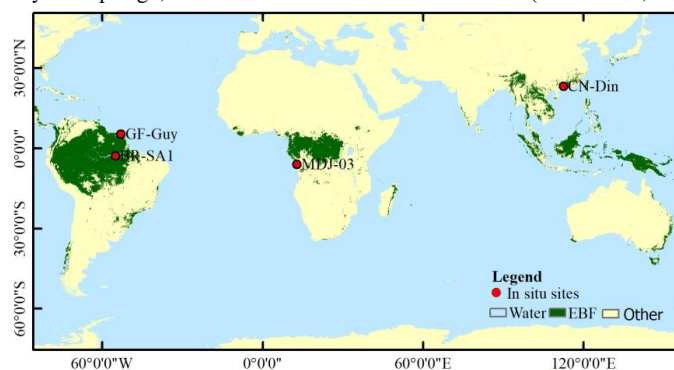
120 **Figure 1.** Tropical and subtropical broadleaved evergreen forests (TEFs) and in situ observation sites. The
121 studied TEFs is determined as those labeled as evergreen broadleaf forest (EBF) from the MODIS land cover
122 maps at a 0.05° spatial resolution. The red dots are in situ observation sites of $V_{c,max25}$.

123
2.2 Data sources for mapping the young leaves $V_{c,max25}$

The continental scale GPP (referred to as RTSIF-derived GPP) at a resolution of 0.125° and spanning
from 2001 to 2018 was derived from TROPOMI (Tropospheric Monitoring Instrument) SIF data, according
to the relationships between the SIF and GPP delineated by Chen et al. (2022), which used a constant value
of 15.343 to transform the SIF to the GPP (see **Sect. 2.4.1**). Monthly meteorological data, including the air
temperature (T_{air}) from the ERA5-Land dataset (Zhao et al., 2020), vapor pressure deficit (VPD) from ERA-
Interim (Yuan et al., 2019), and downward shortwave solar radiation (SW) provided by the Breathing Earth
System Simulator (BESS; Ryu et al., 2018), were used to calculate the Michaelis–Menton constant for
carboxylase (K_C), the Michaelis–Menton constant for oxygenase (K_0), the CO_2 compensation point (г*), dark
respiration (R_d), and thus to calculate the An parameter according to the equations in **Table S4** (see the
Supplement). All datasets were collected and harmonized to a spatial resolution of 0.125°. Further details
regarding the satellite and input data are provided in **Table 1**.

Table 1. Data sources for mapping the $V_{c,max25}$ of young leaves across tropical and subtropical broadleaved evergreen forests

Data name and Abbr.	Source	Usage	Spatial resolution	Temporal resolution	Temporal coverage
Temperature (T_{air})	ERA5-Land	Calculate the K_C, K_0, г*, and R_d for An	0.1° × 0.1°	Monthly	2001.1-2018.12
Shortwave solar radiation (SW)	BESS	Calculate the J_e for An	0.05° × 0.05°	Monthly	2001.1-2018.12
Vapor pressure deficit (VPD)	ERA5-Land	Calculate the C_i for An	0.1° × 0.1°	Monthly	2001.1-2018.12
Sun induced chlorophyll fluorescence (RTSIF)	TROPOMI SIF	RTSIF-derived GPP	0.05° × 0.05°	Monthly	2001.1-2018.12
Gross primary production retrieved from OCO-2 Solar induced chlorophyll fluorescence (GOSIF)	GOSIF	GOSIF-derived GPP	0.05° ×0.05°	Monthly	2001.1-2018.12
Gross primary production from eddy covariance flux tower measurements (FLUXCOM)	FLUXCOM	FLUXCOM-derived GPP	0.5° × 0.5°	Monthly	2001.1-2013.12
Leaf-age-dependent leaf area index seasonality product (Lad-LAI)	Yang et al., 2023	Dissolved $V_{c,max25}$ from GOSIF-derived GPP	0.25° × 0.25°	Monthly	2001.1-2018.12

138
2.3 Data for validating the young leaves $V_{c,max25}$

The $V_{c,max25}$ of the young and mean leaves age from in situ observations were collected to validate the
$V_{c,max25}$ seasonality simulated from RTSIF-derived GPP by the proposed model (**Table S1**). Monthly young
leaves and mean leaves age $V_{c,max25}$ observations occurred between August and December 2012 at the
Santarem Primary Forest Ecosystem Research Station (BR-Sa1) sites (Albert et al., 2018). The annual mean
leaves age $V_{c,max25}$ observations were acquired over 12 months during the period of 2004 to 2016 at the

145 Guyaflux Forest Ecosystem Research Station (GF-Guy) sites (Wang et al., 2022) and from 2003 to 2009 at
146 the Dinghushan Forest Ecosystem Research Station (CN-Din) sites (https://fluxnet.org/data/fluxnet2015-
147 dataset/), and in November 2012 at the Mbam–Djerem National Park 3 (MDJ-03) sites (Ishida et al., 2015).
148 The data regarding the young leaves and mean leaves age $V_{c,max25}$ for the BR-Sa1 site were obtained directly
149 from the literature, whereas the remaining three sites were sourced solely through existing literature,
150 providing only the mean leaves age $V_{c,max25}$ for each. To evaluate the simulated young leaves $V_{c,max25}$, the
151 dissolved method (see **Sect. 2.5.1**) was employed to compute the young leaves $V_{c,max25}$ as the true values in
152 accordance with the Lad-LAI product (Yang et al., 2023). A monthly leaf-age-dependent leaf area index
153 product (referred to as Lad-LAI) at 0.25° spatial resolution over the continental scale during 2001-2018,
154 developed by Yang et al. (2023), was used to derive $V_{c,max25}$ through the dissolved method (see **Sect. 2.5.1**)
155 from the GOSIF-derived GPP, with the aim of evaluating the efficiency and reliability of the newly proposed
156 methodology. Furthermore, Gross primary production retrieved from OCO-2 Solar induced chlorophyll
157 fluorescence (referred to as GOSIF-derived GPP) data for the period spanning from 2001 to 2018, with a
158 resolution of 0.05°, and Gross primary production from eddy covariance flux tower measurements (referred
159 to as FLUXCOM-derived GPP) data for the period between 2001 and 2013, with a resolution of 0.5°, were
160 also used to test the uncertainty of the proposed model for the simulation of monthly gridded young leaf
161 $V_{c,max25}$ (**Table 1**).
162
163 **2.4 Methods for simulating the young leaves $V_{c,max25}$**
164   **Fig. 2** shows the practical procedures applied to produce the seasonal dynamic product of the young leaf
165 $V_{cmax,25.}$ The 'leaf demographic-identical (LDO)' hypothesis proposes that the leaf cohorts can be classified
166 into three categories on the basis of their growth, development and lifespan: young leaf (less than 60 days),
167 mature leaf (between 60 days and 180 days), and old leaf (greater than 180 days) (Wu et al., 2017). To ensure
168 comparability between the observations and simulations and simplify the calculations, we categorized the
169 leaf area index (LAI) and the corresponding net CO_2 assimilation rate (An) into two groups based on leaf
170 age: those with a leaf age greater than 180 days were considered 'old,' and those with a leaf age less than 180
171 days were considered 'young' (Chen et al., 2019). Since the total GPP of the leaf cohort remained constant
172 and the leaf cohorts were composed of leaves of different ages, we calculated the total GPP as a linear sum
173 of the GPP of each leaf age cohort. The total GPP was simulated using the FvCB photochemical model by
174 combining the LAI groups (young leaf LAI_Y vs. old leaf LAI_O; **Equation 1**) and the corresponding net
175 assimilation rates of CO_2 (young and mature An_Y vs. old leaf An_O; **Equation 1**) (Farquhar et al., 1980).
176         $LAI_{-Y} \times An_{-Y} + LAI_{-O} \times An_{-O} = GPP_{total}$ (1)
177 where LAI_{-Y} represents the LAI of young leaves (<180 days) and LAI_{-O} represents the LAI of old leaves
178 (>180 days). An_Y and An_O represent the net CO_2 assimilation rates of young and old leaves, respectively.
179 The sum of LAI_{-Y} and LAI_{-O} was set as the total canopy LAI. GPP_{total} refers to the total gross primary
180 production of the canopy.
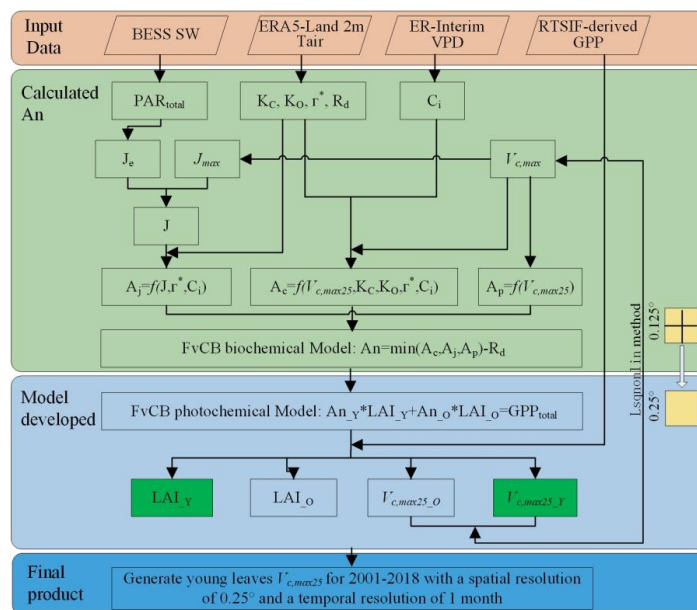
Figure 2. Procedures for mapping the $V_{c,max25}$ of young leaves using a neighbor-based approach.

The gridded GPP data over the whole TEFs were derived from SIF (denoted as RTSIF-derived GPP) using a linear SIF–GPP regression model (see **Sect. 2.4.1**), which was established based on in situ GPP from 76 eddy covariance (EC) sites (Chen et al., 2022). The majority of the tropical and subtropical TEFs retain leaves year-round, and their total LAI shows marginally small spatial and seasonal changes (Wu et al., 2016; **Fig. S2**). Therefore, previous modeling studies have assumed a constant value for the total LAI in tropical and subtropical TEFs (Cramer et al., 2001; Arora and Boer, 2005; De Weirdt et al., 2012). Based on this, we collected observed seasonal LAI dynamics in tropical and subtropical TEFs from previously published literature, which showed a constant value of LAI at around 6.0 (**Fig. S2; Table S3**). Consequently, in this study, we streamlined the data to assume that the seasonal LAI was broadly equivalent to 6.0 in tropical and subtropical TEFs. This assumption was also found to be reasonable in the region of the TEFs by Yang et al. (2023). The LAI_{-O} is equal to $6 - LAI_{-Y}$. The $V_{c,max25}$ values for old cohorts were set to 20 μmol m^{-2} s^{-1} according to previous ground-based observations (Chen et al., 2019; Zhou et al., 2015) in our method The An_{-O} can be calculated according to the FvCB biochemical model (Farquhar et al., 1980; Bernacchi et al., 2003; see **Sect. 2.4.2**). An_{-Y} can be expressed as the function of $V_{c,max25}$ for young leaves (see **Sect. 2.4.2**). Consequently, only LAI_{-Y} and $V_{c,max25}$ of young leaves remains as the final parameters to be solved in **Equation 1**.

The model's complexity is evident due to the two parameters that needed to be solved. To overcome the challenge of the model calculation, we assumed that the four adjacent pixel points had homogeneous plant functional types (PFTs) and had consistent leaf age cohorts. The LAI and $V_{c,max25}$ of young leaves were estimated using nonlinear least squares and constraints on the basis of the GPP values with the four neighboring pixels, according to **Equation 1**. The input gridded dataset consisted of the GPP obtained from the RTSIF and climatic data such as T_{air}, VPD and SW, and the spatial resolution of these data was homogeneously resampled to 0.125°, resulting in a spatial resolution of 0.25° for the map of the output young leaf $V_{c,max25}$. We further validated the robustness and reliability of the neighborhood pixel method by scaling

207   the numbers of the neighborhood pixels, yielding a lower spatial resolution version, $V_{c,max25}$ at 0.5°. In the
208   optimization process, an mean $V_{c,max25}$ value was determined by assuming that the leaf cohort was completely
209   young. A reasonable adjustment for the young leaf $V_{c,max25}$ value was then determined based on previously
210   published literature (Chen et al., 2022; Yang et al., 2023) and the initial value. Importantly, the difference
211   between the finely optimized young leaf $V_{c,max25}$ value and the initial value could often be significant and
212   outside the margin of error. Therefore, an appropriate adjustment for the young leaf $V_{c,max25}$ value needs to be
213   carefully determined (He et al., 2019). All analyses were performed using MATLAB (R2 version).

214

215   **2.4.1 Calculating the GPP (RTSIF-derived GPP) from TROPOMI SIF**

216   SIF is a widely used proxy for canopy photosynthesis (Yang et al., 2015; Dechant et al., 2020). Here,
217   we used a long-term reconstructed TROPOMI SIF dataset (RTSIF; Chen et al., 2022) to estimate GPP
218   seasonality. Previous analyses showed that RTSIF was strongly linearly correlated to eddy covariance (EC)
219   GPP and used 15.343 as a transformation coefficient to convert RTSIF to GPP (Chen et al., 2022). We
220   collected seasonal GPP data observed at four EC sites from the FLUXNET2015 tier 1 dataset (**Table S2**;
221   Pastorello et al., 2020) and validated the Chen et al. (2022) simple SIF–GPP relationship (**Fig. S1** in the
222   Supplement). Results confirmed the robustness of the Chen et al. (2022) simple SIF–GPP relationship for
223   estimating the GPP seasonality in tropical and subtropical TEFs (R>0.49). Despite the potential
224   overestimation (**Fig. S1f**) or underestimation (**Fig. S1h**) of the magnitudes, the RTSIF-derived GPP mostly
225   captured the seasonality of the EC GPP at all four sites (d_{phase} < 0.29).

226

227   **2.4.2 Calculating the net CO2 assimilation rate**

228   The net CO_2 assimilation rate is a significant parameter characterizing the photosynthetic rate.
229   According to Farquhar's (1980) biochemical model (FvCB), the net CO_2 assimilation rate (An) depends on
230   the most limiting conditions for photosynthesis (RuBisCO saturation A_c, RuBP saturation A_j, or TPU
231   saturation A_p) and the intensity of dark respiration (R_d, Bernacchi et al., 2013). The net CO_2 assimilation rate
232   (either An_Y or An_O) can be expressed by the following equation:

233   $$An = \min(A_c, A_j, A_p) - R_d \tag{2}$$

234   **(1) Calculation of Ac**

235   When the CO_2 pressure is low (C_i<300 µmol mol^{-1}), the net photosynthesis rate is mainly constrained
236   by the activity and quantity of the carboxylase RuBisCO. The Rubisco-limited photosynthetic rate A_c can be
237   calculated using the following equation under a limited carboxylation rate:

238   $$A_c = V_{cmax} \times \frac{C_i - \Gamma^*}{C_i + K_c \times (1 + \frac{O}{K_0})} \tag{3}$$

239   where Γ^* represents the CO_2 compensation point and C_i is the intercellular CO_2 pressure. K_c, K_0, O, and
240   Γ^* are estimated based on the leaf temperature using **Equation 4** to calculate their values at the given
241   temperature, which is used to convert from their values at 25°.

242   $$P = P_{25} \times e^{\frac{(T_k - 298.15) \times \Delta H_p}{r \times T_k \times 298.15}} \tag{4}$$

243   where P is the parameter at each temperature that varies with temperature, including the Michaelis constant
244   for O_2 (K_0), the Michaelis constant for CO_2 (K_0), the intercellular concentration (O) and the CO_2
245   compensation point (Γ^*). P_{25} denotes the constant temperature dependence parameter at 25°C (Bernacchi et
246   al., 2001); specifically, K_c, K_0, T and O at 25°C are equal to 404.9 µmol mol^{-1}, 278.4 mmol mol^{-1}, 42.75 µmol
247   mol^{-1} and 210 mmol mol^{-1}, respectively. ΔH_p is the activation energy, which varies with the temperature and
248   parameters. r is the standard gas constant (8.314 J mol^{-1} K^{-}). T_k is the leaf temperature (unit: Kelvin).

249   Using the stomatal conductance model, the internal CO_2 concentration (C_i, **Equation 5**) was estimated
250   to depend on the atmospheric CO_2 concentration instead of the ambient relative moisture (Xu et al. 2017; Lin

251 et al., 2015; Medlyn et al., 2011).

$$C_i = 380 \times (1 - \frac{1}{1.6 \times (1 + \frac{3.77}{\sqrt{VPD}})}) \tag{5}$$

253 where C_i represents the internal CO_2 concentration and VPD denotes the vapor pressure deficit data in hPa.

254 **(2) Calculation of Aj**

255 When the concentration of CO_2 is high, leaf photosynthesis is constrained by RuBP regeneration. The

256 photosynthetic rate (A$_j$) is then limited by electron transport and calculated using the following equation:

$$A_j = J \times \frac{C_i - \Gamma^*}{4 \times (C_i + 2 \times \Gamma^*)} \tag{6}$$

258 where J is the electron transport rate for leaf photosynthesis limited by light. It is a quadratic function of the

259 full electron transfer rate (J_e) and maximum electron transfer rate (J_{max}) (Bernacchi et al., 2013; Luo et al.,

260 2001). The maximum electron transport rate (J_{max}), the maximum carboxylation rate ($V_{c,max25}$), and the CO_2

261 compensation point in the absence of mitochondrial respiration (Γ^*) were used to determine the Michaels–

262 Menten constants for oxygenation and carboxylase. For the detailed calculation process, refer to **Equations**

263 **7-9**.

$$J = \frac{J_e + J_{max} - \sqrt{(J_e + J_{max})^2 - 4 \times J_e \times J_{max} \times \theta}}{2 \times \theta} \tag{7}$$

$$J_e = PAR_{total} \times \partial \times \varphi \times \kappa \tag{8}$$

$$J_{max} = J_{max,25} \times e^{((\frac{25 - T_{opt}}{\Phi})^2 - (\frac{T_k - 273.15 - T_{opt}}{\Phi})^2)} \tag{9}$$

267 where J_{max} denotes the maximum electron transfer rate at a given temperature and varies with temperature.

268 $J_{max,25}$ is the maximum electron transfer rate at 25°C, is usually assigned $1.67 \times V_{c,max25}$ in TEFs. T_{opt} and

269 T_{air} are the optimum temperature for electron transfer and the leaf temperature, respectively. J_e is a

270 function of canopy photosynthetically active radiation (PAR_{total}) and can be calculated by inputting SW and

271 LAI; for details, refer to Weiss and Norman (1985) and Ryu et al. (2018). θ, ∂, φ, and Φ are constants

272 and equal to 0.7, 0.85, 0.5, and 0.85, respectively (Xu et al., 2017; Yang et al., 2023). κ is a function of the

273 optimal temperature, which is the maximum quantum efficiency of PSII photochemistry.

274 **(3) Calculation of Ap**

275 The rate of photosynthesis is limited by the export of triose phosphate. A$_p$ represents the photosynthetic

276 capacity to export or utilize the photosynthetic products for the different LAI cohorts, as determined by

277 multiple on-site observations.

$$A_p = c \times V_{c,max25} \tag{10}$$

279 The ratio of the interior foliar CO_2 concentration to the environmental CO_2 concentration was fixed at

280 0.5 for C3 species and 0.7 for C4 species based on previous investigations. (Fabre et al., 2019; McClain et

281 al., 2019; Yang et al., 2016).

282

283 **2.5 Methods for evaluating the simulated young leaves $V_{c,max25}$**

284 This study assessed the proposed algorithms in three ways: (1) monthly observed $V_{c,max25}$ through in situ

285 measurements, which were collected from the literature; (2) yearly dissolved $V_{c,max25}$ from the GOSIF-derived

286 GPP; and (3) monthly Lad-LAI product dependent on new leaf age covering the entire TEF region; these

287 were obtained from the RTSIF product by Yang et al. (2023). However, the in situ $V_{c,max25}$ of young leaves

288 remains an unfulfilled need, only one site (BR-Sa1; see **Sect. 2.3**) of annual monthly young leaves $V_{c,max25}$ is

289 available. In order to compensate for the lack of ground-based validation, three sites (GF-Guy, MDJ-03, CN-

290 Din) of the seasonality $V_{c,max25}$ of mean leaves age were also collected and calculated the young leaves $V_{c,max25}$

291 using the dissolved method (see **Sect. 2.5.1**) based on the Lad-LAI product (Yang et al., 2023). To evaluate

292 the efficiency and reliability of the newly proposed methodology, a comparison was also conducted between

293 the grid young leaves $V_{c,max25}$ simulated from RTSIF-derived GPP by using the newly proposed method and

294 that dissolved from GOSIF-derived GPP and the Lad-LAI product by using dissolved method. To investigate

295 the reliability of the neighborhood-based subdivision technique, we conducted a comparative analysis of the

296   young leaves $V_{c,max25}$ derived from RTSIF-derived GPP using 2×2 (0.25° resolution) and 4×4 (0.5°resolution)
297   neighboring pixels. To assess the uncertainties stemming from the estimation of gross primary productivity
298   (GPP), we incorporated two additional GPP products, GOSIF-derived GPP and FLUXCOM GPP (Jung et al.,
299   2019; Yang et al., 2023), along with the original RTSIF-derived GPP, resulting in three distinct versions of
300   the young leaves $V_{c,max25}$ products.

301

302   **2.5.1 Dissolved method for evaluating the young leaves $V_{c,max25}$**
303   The total GPP can be expressed as the sum of the GPP of the old and young leaf age cohorts. The GPP
304   of each leaf age cohort is a function of the corresponding LAI cohort and net CO_2 assimilation rate. In
305   accordance with related studies, the $V_{c,max25}$ of old leaves is presumed to be a constant value (Chen et al.,
306   2020). When the LAI of different leaf ages is known, only the $V_{c,max25}$ of the young leaves remains unknown
307   in **Equation 1**. The value of the $V_{c,max25}$ of the young leaves can be determined by solving the aforementioned
308   **Equation 1**. This method involves dividing GPP into old and young GPP according to leaf age, with the
309    $V_{c,max25}$ of young leaves being directly solved by using the Lad-LAI product, hence the term 'dissolved
310   method'. At present, there is a lack of available data regarding the ground $V_{c,max25}$ of different leaf ages. The
311   dissolved method is employed to validate the reasonableness of the proposed algorithm.

312

313   **2.5.2 K-means method for classification of the young leaves $V_{c,max25}$**
314   We analyzed the spatial patterns of $V_{c,max25}$ across TEFs using the K-means clustering analysis. K-means
315   algorithm is an iterative algorithm that tries to partition the dataset into K predefined distinct non-overlapping
316   subgroups (clusters) where each data point belongs to only one group. It tries to make the intra-cluster data
317   points as similar as possible while also keeping the clusters as different (far) as possible. It assigns data points
318   to a cluster such that the sum of the squared distance between the data points and the cluster's centroid
319   (arithmetic mean of all the data points that belong to that cluster) is at the minimum. The less variation we
320   have within clusters, the more homogeneous (similar) the data points are within the same cluster. The way k-
321   means algorithm works is as follows:
322   (1)   Specify number of clusters K.
323   (2)   Initialize centroids by first shuffling the dataset and then randomly selecting K data points for the
324   centroids without replacement.
325   (3)   Keep iterating until there is no change to the centroids. i.e. assignment of data points to clusters isn't
326   changing.
327   (4)   Compute the sum of the squared distance between data points and all centroids.
328   (5)   Assign each data point to the closest cluster (centroid).
329   (6)   Compute the centroids for the clusters by taking the average of the all data points that belong to each
330   cluster.

331

332   **2.5.3 Precision evaluation index**
333   Both the root mean square error (RMSE, **Equation 11**) and Pearson's correlation coefficient (R,
334   **Equation 12**) were employed to evaluate the model capabilities.

335
$$RMSE = \sqrt{\frac{\sum_{i=1}^{N}(V_i - U_i)^2}{N}} \tag{11}$$

336
$$R = \frac{\sum_{i=1}^{N}(V_i - \bar{V})(U_i - \bar{U})}{\sqrt{\sum_{i=1}^{N}(V_i - \bar{V})^2}\sqrt{\sum_{i=1}^{N}(U_i - \bar{U})^2}} \tag{12}$$

$$SD_S = \sqrt{\frac{1}{N}\sum_{i=1}^{n}(V_i - \bar{V})^2} \tag{13}$$

$$SD_m = \sqrt{\frac{1}{N}\sum_{i=1}^{n}(U_i - \bar{U})^2} \tag{14}$$

$$LCS = 2SD_S SD_m(1 - R) \tag{15}$$

where N is the total point extracted from the $V_{c,max25}$ products simulated from RTSIF-derived GPP; V_i and U_i represent the monthly simulated and observed in situ measurements $V_{c,max25}$, respectively; and $\bar{\bar{V}}$ and $\bar{\bar{U}}$ are the mean values of the simulated and observed in situ measurements $V_{c,max25}$. Moreover, the continental $V_{c,max25}$ simulated from the proposed model was compared against that the dissolved from GOSIF-derived GPP and Lad-LAI over the TEF regions. SD_S is standard deviation of the simulation, and SD_m is the standard deviation of the measurement. And the lack of correlation weighted by the standard deviations (phase-related difference; d$_{phase}$; d$_{phase}$ = LCS).

3. Results

3.1 Validation of the gridded $V_{c,max25}$ seasonality of young leaves using in situ observations

The seasonality of simulated mean $V_{c,max25}$ of all canopy leaves and $V_{c,max25}$ of young leaves was evaluated with in situ measurements at 4 sites: CN-Din site in southern China (Latitude: 23.170°N; Longitude: 112.540°E), MDJ-03 site in Congo (Latitude: 5.984°S; Longitude: 12.869°E), and BR-Sa1 (Latitude: 2.8567°S; Longitude: 54.958°W) and GF-Guy (Latitude: 5.278°N ; Longitude: 52.925°W) sites in southern America. Overall, the estimated mean $V_{c,max25}$ of all canopy leaves (black line) ranged from 20 µmol m^{-2} s^{-1} to 60 µmol m^{-2} s^{-1}, and their seasonal fluctuations agreed well with the in situ mean $V_{c,max25}$ (red dots) (**Fig. 3**). In contrast, $V_{c,max25}$ (green line) of the young leaf cohorts (green line) exhibited higher values compared with those of all canopy leaves, ranging from between 40 µmol m^{-2} s^{-1} and 80 µmol m^{-2} s^{-1}. This finding is consistent with previous studies that young leaves were more photosynthetically effective than old leaves (Urban et al., 2008; Albert et al., 2018; Menezes et al., 2022). Specifically, our simulations can capture well the various seasonal patterns of $V_{c,max25}$ across different sites. At the BR-Sa1 site, the estimates were correlated well with the observed mean $V_{c,max25}$ for all (R=0.85) and young leaves (R=0.84), which both increased during the dry season (approximately between June December) (**Fig. 3a, 3b**). At the GF-Guy site, in situ mean $V_{c,max25}$ of all canopy leaves showed considerable seasonality, while $V_{c,max25}$ of young leaves remain much stable (**Fig. 3c**). Our estimates also performed well in simulating the $V_{c,max25}$ of all canopy leaves (R=0.95) and that of young leaves (R=0.66) (**Fig. 3d**). In contrast, at the Din site in subtropical Asia, both $V_{c,max25}$ for all canopy leaves and young leaves increased during the wet-season period, with the highest precipitation occurring in June or July (**Fig. 3e**). This is similar in the Congo-MDJ3 site, where both $V_{cmax,25}$ for all canopy leaves and young leaves also increased during the wet-season period but with larger seasonal variations. Our model showed the best simulations of $V_{c,max25}$ of young leaves in Din site (all canopy leaves: R=0.84; young leaves: 0.95). Nevertheless, many more long-term in situ measurements are needed to determine the reliability of these time series fluctuations.

Then, we analyzed the spatial patterns of $V_{c,max25}$ across TEFs using the K-means clustering analysis. Results showed that $V_{c,max25}$ for young leaf cohorts in tropical forests had evident seasonal dynamics, bringing influences on canopy photosynthesis. **Fig. S3** shows the seasonal fluctuations in $V_{c,max25}$ for the young leaves in ten individual regions, as clustered using K-means analysis. In the middle and southern regions of the Amazon, the young leaf $V_{c,max25}$ decreased with the onset of the wet season (approximately February) and conversely increased with the onset of the rainy season (approximately June). In contrast, in subtropical Asia, the young leaf $V_{c,max25}$ increased during the wet season, peaking in June or July when rainfall was highest. Near the equator, the young $V_{c,max25}$ showed a bimodal seasonality with very slight variations.

380
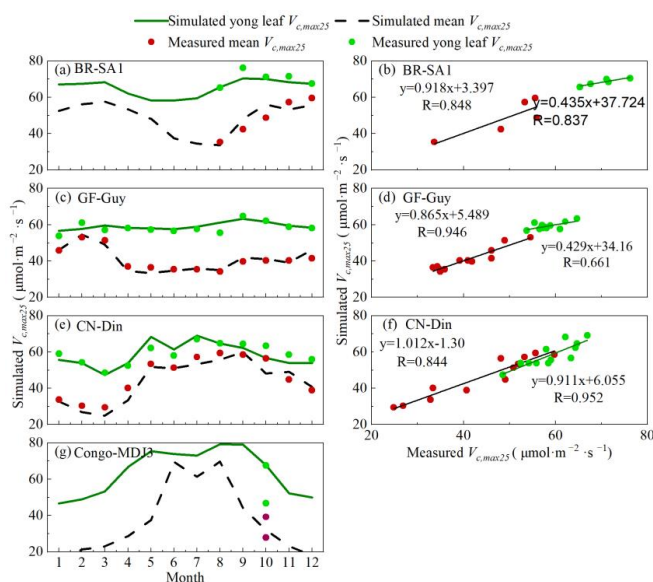
Figure 3. Validations of simulated seasonal $V_{c,max25}$ for all canopy leaves and young leaves with in situ observations. The green lines and green dots are the seasonal young leaf $V_{c,max25}$ simulated from RTSIF derived GPP by the proposed method. The black line and red dots are the mean leaf age $V_{c,max25}$ values from the simulations and in situ observations, respectively. Simulated $V_{c,max25}$ denoted as the young leaf $V_{c,max25}$ simulated from RTSIF-derived GPP by using the new proposed method. Mean $V_{c,max25}$ denoted as the mean leaves age $V_{c,max25}$.

3.2 Validation of the young leaves $V_{c,max25}$ simulated from RTSIF-derived GPP against that dissolved from GOSIF-derived GPP

The $V_{c,max25}$ of young leaves simulated from RTSIF-derived GPP demonstrated significantly correlations (R ranges from 0.512 to 0.870) with those dissolved from GOSIF-derived GPP (**Fig. 4a-j**). However, notable discrepancies remained between these two independent $V_{c,max25}$ estimates (**Fig. 5**). Statistically, the seasonally young leaf $V_{c,max25}$ simulated from RTSIF-derived GPP exhibited strong correlations with those dissolved from the GOSIF-derived GPP (R>0.80) across 86.34% of the entire TEFs area, with a mean correlation coefficient of 0.87 (**Fig. 5a-c**). And the RMSE remained below 11.591 for 91.68% of the TEFs (**Fig. 4d-f**). Nevertheless, this correlation varies across sub-regions. The K-means spatial clustering analysis showed that $V_{c,max25}$ of young leaves simulated from RTSIF-derived GPP was more strongly correlated with the those estimated from the GOSIF-derived GPP in the low-latitudes (Amazon R1 R=0. 903; Amazon R2 R=0.935; Amazon R4 R=0.869; Amazon R5 R=0.767; Congo R6 R=0.905; Congo R7 R=0.965; Asia R8 R=0.860; Asia R9 R=0.841) in comparison to those in the higher latitudes (Amazon R3 R=0.602; Amazon R10 R=0.499). The RMSE results also showed better performance in capturing the seasonality of $V_{c,max25}$ in the low-latitude regions (Amazon R1 RMSE=1.779; Amazon R2 RMSE=2.169; Amazon R4 RMSE=4.668; Congo R6 RMSE=3. 262; Congo R7 RMSE=4.726; Asia R8 RMSE=3.378; Asia R9 RMSE=5.861; **Fig. S4**) compared to those in the regions further from the equator at higher latitudes (Amazon R5 RMSE = 14.845; Amazon R10 RMSE = 6.918; **Fig. S5**). However, more in situ measurements are needed to refine and validate the simulated $V_{c,max25}$ product. Despite these obstacles, the present product provides an improvement from the current state of the art and can be immediately applied in parameterizing terrestrial ecosystem models.

408
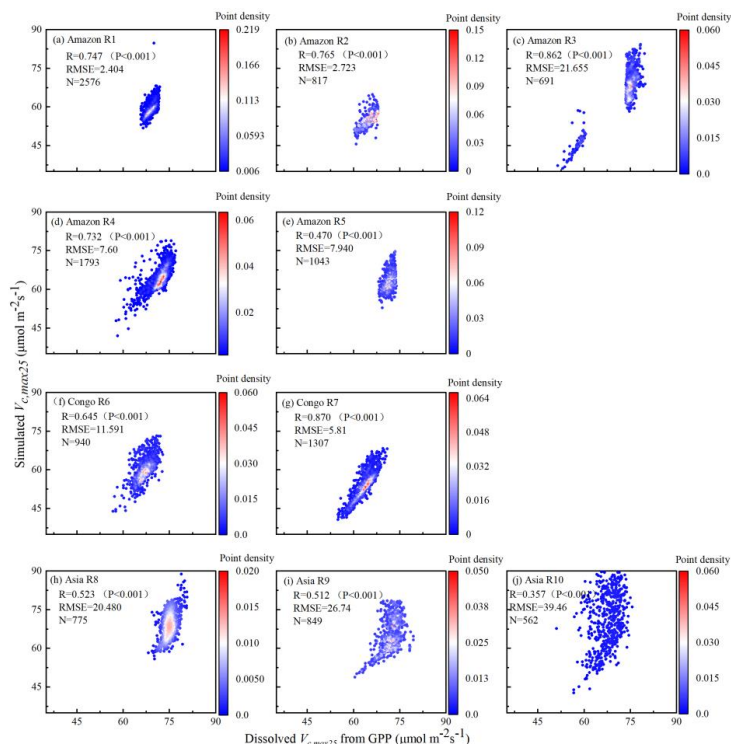
Figure 4. Comparisons of the young leaves $V_{c,max25}$ simulated from RTSIF-derived GPP against that dissolved
from GOSIF-derived GPP

411

412
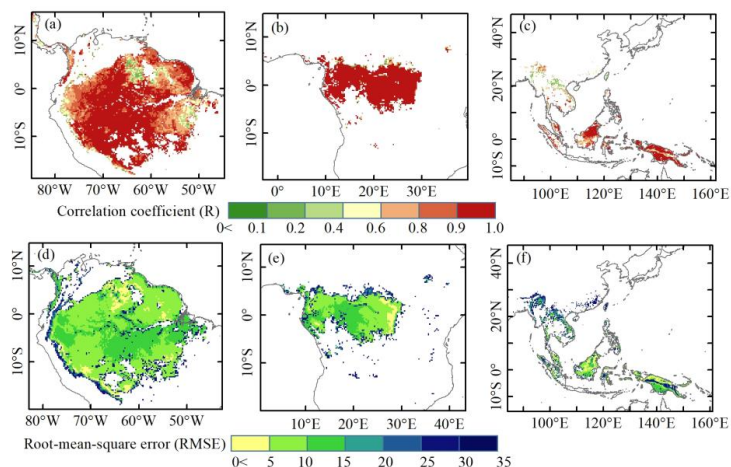
Figure 5. The root mean square error (RMSE) and correlation coefficient (R) between the young leaves
$V_{c,max25}$ derived from RTSIF-derived GPP and that dissolved from GOSIF-derived GPP.

415

3.3 Comparison of the seasonal $V_{c,max25}$ of young leaves with the leaf age product

Field measurements revealed different seasonal patterns of young leaf $V_{c,max25}$ across the TEFs. However, due to the low spatial coverage of in situ observation sites, it still remains challenging to comprehensively and directly assess the their variations. Here, the K-means clustering analysis was performed on the simulated $V_{c,max25}$ maps to investigate its geospatial coherency in comparison with a gridded leaf age product developed by Yang et al. (2023).

The geospatial distribution of the young leaf $V_{c,max25}$ products clustered based on the satellite vegetation signals (**Fig. 6a-c**) was closely matched those of climatic factors classified by the K-means clustering analysis (**Fig. 6d-f**) analyzed by Chen et al. (2021). These distributions were generally comparable to the spatial patterns of the Lad-LAI products clustered based on the endogenous climate variables presented earlier in the maps from Yang et al. (2021) (**Fig. 6g-i**). All these results exhibit similar spatial clustering patterns. In the middle (sub-region R2) and northern (sub-region R3) Amazon (**Fig. 7a**), the seasonal variation in the young leaf $V_{c,max25}$ (**Fig. 8b, c**) was consistent with that of the BR-Sa1 and GF-Guy sites, where young leaves increase during the dry seasons. Moreover, the seasonality of the young leaf $V_{c,max25}$ in subtropical Asia (**Fig. 8f**) was similar to that of Din, where young leaves conversely increase during the wet seasons. The young leaf $V_{c,max25}$ peaked in July in sub-region R10, which was located between sub-regions R8 and R9, where the young leaf $V_{c,max25}$ exhibited a bidirectional phenology (**Fig. 8j**). The other four sub-regions (R1, R2, R7 and R8) were located near the equator. Unlike sub-regions R1, R2, R7 and R8 that were far from the equator, the young leaf $V_{c,max25}$ clustered near the equator showed less seasonal variations. In particular, in these sub-regions close to the equator, the seasonal pattern of the young leaf $V_{c,max25}$ was bidirectional. The first peak occurred in approximately March, while the second peak occurred in August (**Fig. 8a, d, e, g**). These results were in good agreement with previous studies (Li et al., 2021) that reported a single peak at high latitudes and bidirectional seasonality at low latitudes.
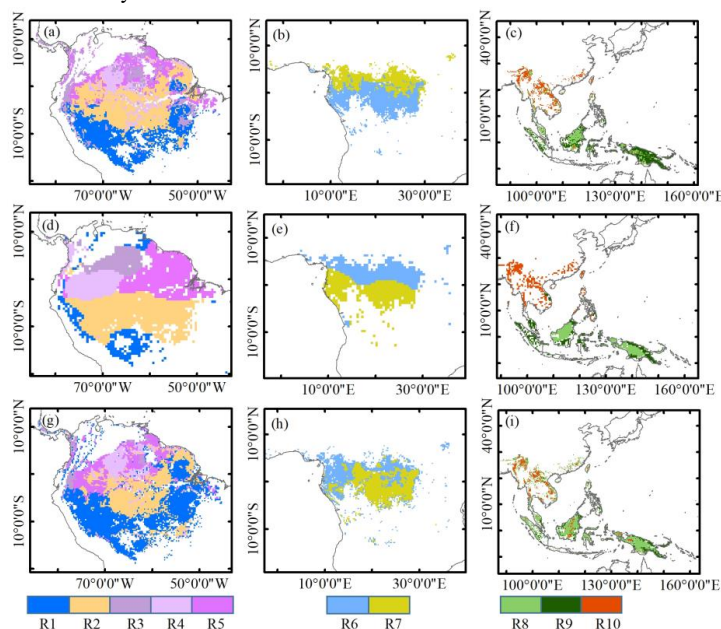
Figure 6. Comparison of sub-regions of the young leaf $V_{c,max25}$ (a-c) with those of climatic factors classified by the K-means clustering analysis (d-f) analyzed by Chen et al. (2021), and those of the Leaf-age-dependent leaf area index seasonality product (Lad-LAI) (g-i) developed by Yang et al. (2023).

443

444
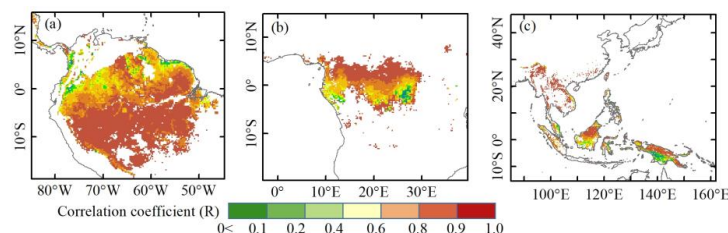
Figure 7. Spatial maps of the correlation coefficient (R) between the monthly simulated $V_{c,max25}$ and the Leaf-age-dependent leaf area index seasonality product (Lad-LAI) developed by Yang et al. (2023).

447

448
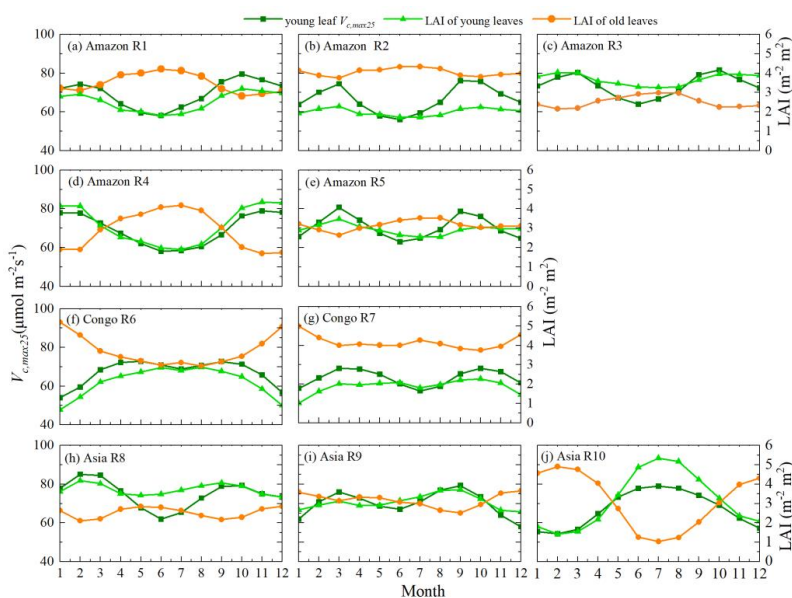
Figure 8. Seasonality of the simulated $V_{c,max25}$ of young leaves in comparison with the Leaf-age-dependent leaf area index seasonality product (Lad-LAI) developed by Yang et al. (2023).

451

3.4 Partial correlations between the seasonal $V_{c,max25}$ of young leaves and individual climatic factors

To assess potential impacts of the climatic seasonality on $V_{c,max25}$ of young leaves, we also conducted spatial clustering analyses on climate factors such as vapor pressure deficit(VPD), air temperature(T_{air}), and downward shortwave solar radiation(SW) (**Fig. 8d-f**), which were found to be key drivers of leaf phenology in TEFs (Li et al. 2021; Yang et al., 2021; 2023). Notably, the spatial patterns of the young leaf $V_{cmax,25}$ generated from satellite-derived vegetation signals (**Fig. 8a-c**), closely matched the patterns derived from independent climate variables such as T_{air}, VPD and SW (see **Fig. 8**). There was a notable positive correlation between the SW and $V_{c,max25}$ across most parts of TEFs (**Fig. 9**). The correlation coefficients exceeded 0.34 in all cases except in the Amazon sub-region R4, where the correlation coefficient was only 0.167. These results highlight the significant role of SW in influencing the canopy photosynthesis in TEF. Although the seasonal fluctuations in temperature were less distinct (**Fig. 10**), possibly due to minor variations in

464 temperature gradients, a substantial positive correlation was observed between the temperature and young
465 leaf $V_{c,max25}$ (**Fig. 9**). This correlation surpassed 0.608 in the Amazon sub-regions R1-R3 and R5 and the Asia
466 sub-regions R9 and R10 (**Fig. S6**). Conversely, a negative correlation, with a mean correlation coefficient of
467 -0.64, was noted in the sub-region R6 of the Congo (**Fig. S6**). These findings were in agreement with earlier
468 investigations and indicated that air temperature significantly impacted the seasonal dynamics of $V_{c,max25}$
469 (Zhou et al., 2015). The relationship between the young leaf $V_{c,max25}$ and VPD considerably varied across the
470 different sub-regions (**Fig. 8**), indicating complex influences of the VPD on canopy photosynthesis in TEFs.
471 This variability was mainly due to the seasonal variations in canopy leaf age, which aged during the rainy
472 season and became rejuvenated during dry seasons (Li et al., 2021; Yang et al., 2021; 2023). As a result, the
473 seasonality of leaf photosynthetic capacity tended to show an inverse trend to the seasonality of the leaf age,
474 as expected (Chen et al., 2020).
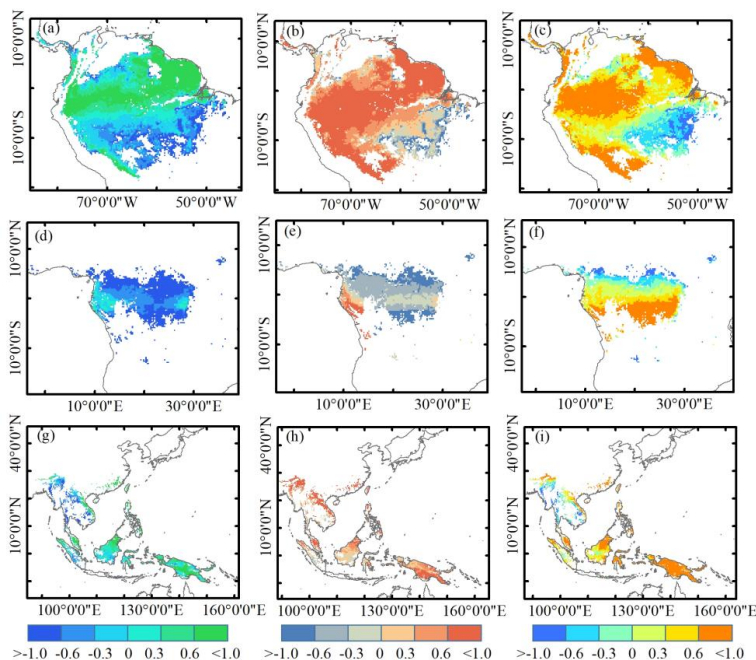
475

476 **Figure 9.** Spatial maps of correlation coefficient (R) between the SIF-simulated monthly $V_{c,max25}$ and climatic
477 and phenological patterns. a, d and g are the spatial maps of correlation coefficient between $V_{c,max25}$ and vapor
478 pressure deficit(VPD); b, e and h are the spatial maps of correlation coefficient between $V_{c,max25}$ and air
479 temperature(T_{air}); c, f and i are the spatial maps of correlation coefficient between $V_{c,max25}$ and downward
480 shortwave solar radiation(SW)

481

482
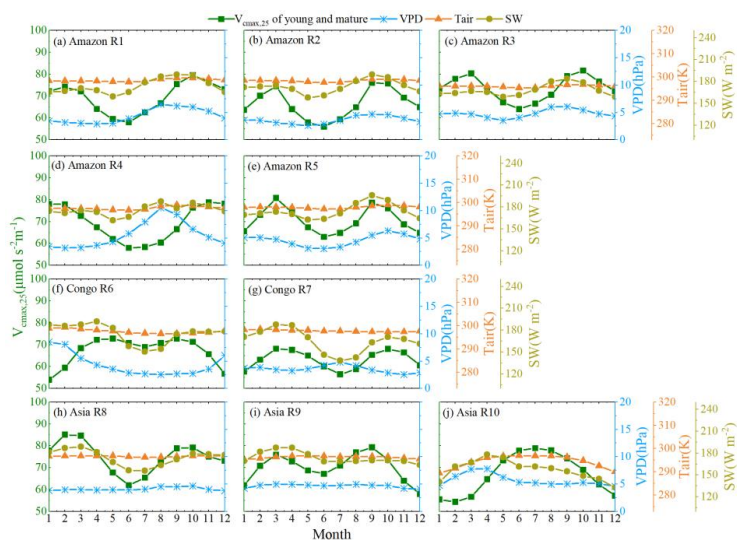
Figure 10. Seasonality of $V_{c,max25}$ of young leaves, air temperature(T_{air}), vapor pressure deficit(VPD) and downward shortwave solar radiation(SW) in the ten sub-regions classified using the K-means clustering analysis method.

486

3.5 Testing potential uncertainties in the young leaves $V_{c,max25}$

The seasonal variations in the young leaf $V_{c,max25}$ using 4×4 neighboring pixels were closely aligned with those observed in the 0.25° products utilizing a grid of 2×2 pixels (**Fig. S7**). Results showed a highly linear correlation between the simulated 0.25° resolution and 0.5°resolution consistent (R>0.995), with the root mean square error (RMSE) being maintained below 0.66 (**Fig. 11**). This evidence supported the concept that the neighbor-based decomposition approach was both robust and dependable for producing the $V_{c,max25}$ products at various spatial resolutions.

Three differentiated versions of the young leaves $V_{c,max25}$ products were produced from RTSIF-, GOSIF- and FLUXCOM-derived GPP at various spatial resolutions (**Figs. S8-10**). Despite minor differences, all these $V_{c,max25}$ products exhibited high spatial correlations (**Fig. 12**). Notably, all three products demonstrated remarkable similarities in the overall geographic patterns (R ranged from 0.87 to 0.963, $P < 0.001$) (**Fig. 13**). The seasonality of the simulated $V_{c,max25}$ from various GPP products aligned well across all the ten sub-regions (**Fig. 12**). By comparing these datasets with the in situ observation sites, we found that the $V_{c,max25}$ generated from RTSIF-derived GPP had the highest correlation and a minimal deviation against the in situ measurements, with R equal to 0.85 and RMSE equal to 13.69 (**Fig. 13**). Overall, all three versions of the young leaf $V_{c,max25}$ products demonstrated consistent seasonal variability and effectively performed across the ten sub-regions.

504
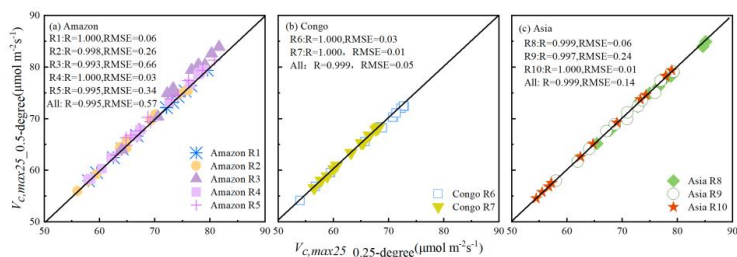
Figure 11. Scatter plots between the simulated $V_{c,max25}$ of young leaves simulated using the 2×2 (0.25° resolution) and 4×4 (0.5° resolution) neighboring pixels in the above-mentioned ten clustered sub-regions.
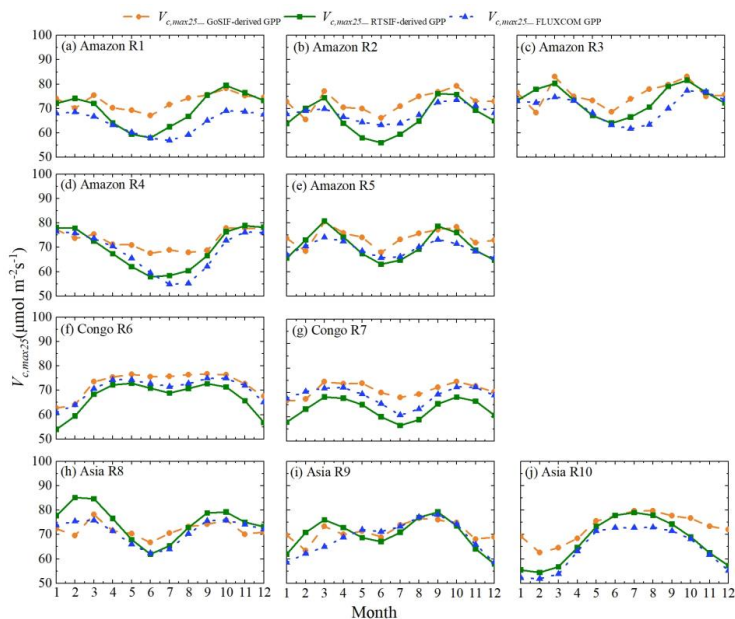
Figure 12. Seasonality of the simulated young leaf $V_{c,max25}$ derived from RTSIF-, GOSIF- and FLUXCOM-derived GPP in the above-mentioned ten clustered sub-regions.
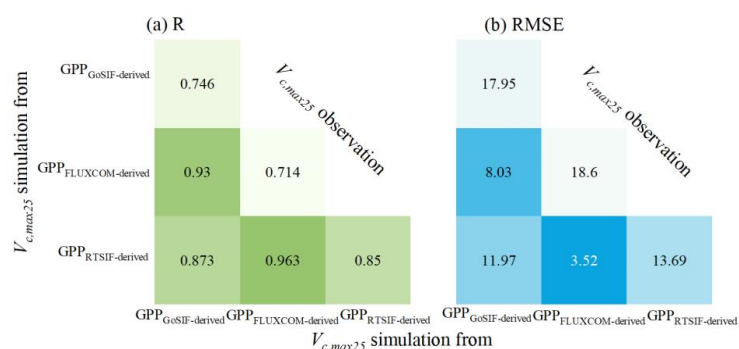
Figure 13. Comparison of RTSIF-derived $V_{c,max25}$ with GOSIF-derived $V_{c,max25}$ (left bottom panels); FLUXCOM-derived $V_{c,max25}$ with RTSIF-derived $V_{c,max25}$ (middle bottom panels); RTSIF-derived $V_{c,max25}$ with FLUXCOM-derived $V_{c,max25}$ (left middle panels); and the three derived $V_{c,max25}$ with the in situ observations (diagonal panels). (a) Correlation coefficients (R); (b) Root mean square error (RMSE).

4. Discussion

Tropical forests, marked by no obvious seasonal shifts in greenness but distant variations in leaf age cohorts (Luo et al., 2021; Zhao et al., 2019; Walther et al., 2019), show distinct leaf phenology compared with temperate and boreal forests. The young leaves are the main leaf cohort to influence photosynthesis

522 (Oliveira et al., 2023; Sharma et al., 2017; Antwi-Boasiako et al., 2011), as previous studies showed that the
523 photosynthesis rates decrease with leaf aging (Menezes et al., 2022; Wang et al., 2020). Thus, understanding
524 the mechanism by which the leaf age influences photosynthesis is crucial for assessing plant growth,
525 ecosystem primary productivity, and the carbon cycle in evergreen forests. (Albert et al., 2018). The leaf
526 carboxylation capacity ($V_{c,max25}$) is crucial for estimating the photosynthetic CO_2 absorption in tropical forests
527 within ESMs. However, most ESMs currently adopt either a single static or an average annual value to
528 represent the $V_{c,max25}$ for each plant functional type (Stocker et al., 2020; Spafford et al., 2023). This empirical
529 practice causes uncertainties in tropical forest biomes, which are characterized by their extensive plant
530 functional diversity (Echeverría-Londoño et al., 2018; Spicer et al., 2022) and variable photosynthetic
531 capacity (Piao et al., 2019; Pinheiro et al., 2023). Additionally, $V_{cmax,25}$ for a certain plant species can also
532 vary significantly with leaf aging, ambient growth temperatures, and the availability of water and nutrients
533 (Stefanski et al., 2022 Lu et al., 2022; Crous et al., 2022;). Thus, seasonal variations in the photosynthesis in
534 tropical evergreen forests are impacted by the turnover of old leaves with low $V_{c,max25}$ values and their
535 replacement by new leaves with higher $V_{c,max25}$ values (Wang et al., 2021; Murphy et al., 2020; Abdul et al.,
536 2016). These findings highlight the importance of accurately quantifying the leaf age and integrating the leaf
537 age information when estimating $V_{c,max25}$ to improve the modeling of the leaf CO_2 assimilation in tropical
538 forests. However, to the best of our knowledge, to date, no comprehensive continental-scale data are available
539 on the leaf age-dependent $V_{c,max25}$ variations throughout tropical evergreen forests. This data gap remains
540 because these variations cannot be adequately mapped by the limited field observations (Hakala et al., 2019)
541 or reliably modeled by ESMs that depend on uncertain climatic variables (Brunner et al., 2021). These
542 challenges prevent researchers worldwide from using remote sensing techniques and land surface models
543 (LSMs) to accurately model the seasonality of large-scale photosynthesis (GPP) (Krause et al., 2022).

544   In this study, we for the first time to provide the continental-scale monthly gridded $V_{cmax,25}$ of young
545 leaves. Based on the newly developed $V_{c,max25}$ product. Additionally, the seasonality of the young leaf $V_{c,max25}$
546 has been effectively evaluated at four locations—CN-Din site in southern China, MDJ-03 site in Congo, and
547 BR-Sa1 and GF-Guy sites in southern America—using the precise, detailed records of the young leaf $V_{c,max25}$.
548 To evaluate the reliability of the gridded young leaf $V_{cmax,25}$ across the entire TEFs, the seasonality of the
549 young leaf $V_{c,max25}$ was also validated pixel by pixel using the dissolved method from the gridded GPP and
550 the leaf age product developed by Yang et al. (2021). The results demonstrated a substantial variation in the
551 $V_{c,max25}$ with leaf age, with observed fluctuations (ranging from 40 μmol m^{-2} s^{-1} to 90 μmol m^{-2} s^{-1}) closely
552 aligning with variations outlined for tropical and subtropical regions in current ESMs, as described by Rogers
553 (2014). These results show the critical need for including age-dependent variations of the $V_{c,max25}$ in future
554 ESM designs. Additionally, the $V_{c,max25}$ values derived from the combined leaves of these updated
555 photosynthesis products can effectively capture the widespread greening of the canopy leaves during the dry
556 season north of the equator. This represents a significant improvement in our capacity to promptly assess and
557 potentially map the $V_{c,max25}$ with high spatial and temporal accuracy in tropical forests. The robustness of
558 these new photosynthesis products has been supported through both direct and indirect assessments.

559   Importantly, in equatorial regions characterized by high annual rainfall, no marked dry seasons typically
560 occur. As a result, variations in the tree canopy phenology are subtler than those observed at higher latitudes
561 (Yang et al., 2021). In these areas, $V_{c,max25}$ of the leaf cohorts display a bimodal phenology pattern with
562 minimal seasonal fluctuation, a phenomenon that is effectively captured by the newly developed
563 photosynthesis product. To convert the SIF data into GPP, a constant coefficient was used, and $V_{cmax,25}$ was
564 assumed to be uniformly distributed across all tropical evergreen forests, potentially introducing further
565 uncertainties. This assumption was reflected in the MSD assessment, where the bias component was

566 predominant, especially near the equator. Nevertheless, the impact of this on the seasonality of photosynthesis
567 was minima; because the phase-dependent component of the RMSE remained relatively insignificant.

568   The "leaf demographic-identical (LDO)" hypothesis categorizes the leaf cohorts into three distinct age
569 classes: new leaves (from 1 to 60 days), mature leaves (from 60 to 180 days), and old leaves (larger than 180
570 days), with corresponding mean $V_{c,max25}$ values as reported by Wu et al. (2016). To facilitate a more effective
571 comparison between the observations and models, we categorized the leaves into two age groups. Leaf ages
572 greater than 6 months are classified as a distinct old leaf class, as per Harris et al. (2007), while leaf ages less
573 than 6 months are combined into a single young leaf class. Juliane et al. (2021) reported that the average
574 $V_{c,max25}$ of mature plants (60-180 days) was the highest. However, the older age classes had values of 30.4 ±
575 1.2 (234–612 days). The $V_{c,max25}$ of the young leaves was 23% greater than that of old leaves, with minimal
576 fluctuations observed in the latter group. The link between the older leaves and $V_{c,max25}$ is less understood in
577 TEFs due to limited field data (Chen et al., 2020). To address these simulation challenges, we defined $V_{c,max25}$
578 for old leaves as a consistent static value; however, this could lead to inaccuracies in predicting
579 photosynthetic performance. This approach affects the accurate depiction of $V_{c,max25}$ and GPP seasonality in
580 ESMs (De Weirdt et al., 2012). Moreover, additional uncertainties stem from assumptions that neglect the
581 spatial and temporal variations influenced by the plant functional type variability, which shifts with seasonal
582 climate anomalies and varies within close proximity in diverse forest ecosystems. These generalizations
583 could also contribute to inaccuracies in simulating seasonal variations in $V_{c,max25}$. Reflecting the inherent
584 variability in photosynthetic behavior across ages, the data revealed two distinct responses: (1) some species,
585 such as P. tomentosa and P. caimito, showed marked reductions in $V_{c,max25}$ as they aged, whereas (2) others,
586 such as M. angularis and V. parviflora, maintained consistent $V_{c,max25}$ values after peaking. Juliane et al. (2021)
587 reported a modest yet significant correlation between the $V_{c,max25}$ and leaf age due to these contrasting patterns.
588 Variations in the photosynthetic capacity at the ecosystem level could be influenced by factors such as the
589 composition of species and the presence and proportion of different functional groups of plants in the forest.

590   In summary, we have presented a novel approach to develop a gridded dataset that incorporates leaf age
591 sensitivity into the photosynthesis products for TEFs on a continental scale. Although some uncertainties
592 remain, a monthly gridded young leaf $V_{c,max25}$ dataset is provided. This innovation facilitates the development
593 of a comprehensive phenological modeling approach for all TEFs within ESMs, which are traditionally
594 operated at coarser resolutions. These improvements substantially enhance our ability to monitor and
595 mechanistically interpret the variations in the $V_{c,max25}$ of young leaf across various regions and periods,
596 providing essential data for the parameterization and assessment of ESMs. Additionally, as remote sensing
597 technologies continue to advance, we anticipate that the enhanced temporal and spatial resolution of RTSIF-
598 derived GPP will facilitate more accurate mapping of the photosynthesis products in the future.

599

5. Data availability

601   The 0.25 degree time-series $V_{c,max25}$ data from 2001-2018 is presented in this paper as the main dataset.
602 We also provided another two versions of $V_{c,max25}$ generated from GOSIF-derived GPP and FLUXCOM GPP,
603 respectively. The three datasets are available at https://doi.org/10.5281/zenodo.14807414 (Yang et al., 2025).
604 These datasets are compressed in a GeoTiff format, with a spatial reference of WGS84. Each file in these
605 datasets is named as follows: "V$_{cmax25}$_{GPP source}derived_{YYYYMM}.tif".

606

6. Conclusions

608   This study for the first time to develop a monthly gridded dataset of $V_{c,max25}$ of young leaves from 2001
609 to 2018 based on RTSIF data. The $V_{c,max25}$ of young leaves simulated from RTSIF-derived GPP was assessed
610 against in situ observations of the monthly $V_{c,max25}$ records, the $V_{c,max25}$ product dissolved from the GOSIF-

611 derived GPP, and the leaf age product Lad-LAI (Yang et al., 2023). Evaluations from these independent leaf-
612 age-related data demonstrated the reliability of the seasonal $V_{c,max25}$ simulations for the young leaf cohorts.
613 Additionally, the $V_{c,max25}$ of young leaves varied across TEFs. In the middle and southern regions of the
614 Amazon, the young leaf $V_{c,max25}$ decreased with the onset of the wet season (approximately February) and
615 conversely increased with the onset of the rainy season (approximately June). In contrast, in subtropical Asia,
616 the young leaf $V_{c,max25}$ increased during the wet season, peaking in June or July when rainfall was highest.
617 Near the equator, the young $V_{c,max25}$ showed a bimodal seasonality with very slight variations. The $V_{c,max25}$
618 products of young leaves can provide usuaful information to improve our understanding of how tropical and
619 subtropical forests are adapting to ongoing climate change. and can be used to refine the phenology models
620 incorporated into LSMs.

621
622 **Supplement.** The supplement related to this article will be available online at once accepted.

623
624 **Author contributions.** XC designed the research and wrote the paper. XY and QS wrote the draft,
625 debugged algorithms and processed data. LH debugged algorithms and reviewed the paper. All the authors
626 edited and revised the paper.

627
628 **Competing interests.** The authors declare no competing interests.

629
630 **Acknowledgement.** We would like to thank the editor and reviewers for their valuable time in reviewing
631 the manuscript.

632
633 **References**

634 Abdul, Baha, N, H., 2016. Photosynthetic characterisation of tropical and temperate rainforest species.
635 Arora, V. K. and Boer, G. J.: Fire as an interactive component of dynamic vegetation models, J. Geophys.
636   Res.-Biogeo., 110, G02008.
637 Atkin, O, K., Meir, P., Turnbull, M, H., 2014. Improving representation of leaf respiration in large-scale
638   predictive climate–vegetation models. New Phytologist, 202(3): 743-748.
639 Ali, A. A., Xu, C., Rogers, A., Fisher, R. A., Wullschleger, S. D., Massoud, E. C., Vrugt, J. A., Muss, J. D.,
640   McDowell, N. G., Fisher, J. B., Reich, P. B., and Wilson, C. J., 2016. A global scale mechanistic model
641   of photosynthetic capacity (LUNA V1. 0). Geoscientific Model Development, 9(2): 587-606.
642 Albert, L, P., Jin, W. Neill, P., Plinio, B, d, C., Travis, E, H., Edgard, S, T., Valeriy, Y, I., Rafael, S, O., Sabrina,
643   G., Marielle, N, S., R, C, O, J., Natalia, R, C., Rodrigo, d, S., Scott, C, S., Giordane, A, M., Deliane, V,
644   P., Scott, R, S., 2018. Age-dependent leaf physiology and consequences for crown-scale carbon uptake
645   during the dry season in an Amazon evergreen forest. New Phytologist, 219(3): 870-884.
646 Antwi-Boasiako, C., Enninful, R., 2011. Effects of growth medium, a hormone, and stem-cutting maturity
647   and length on sprouting in Moringa oleifera Lam. The Journal of Horticultural Science and
648   Biotechnology, 86(6): 619-625.
649 Bernacchi, C.J., Pimentel, C., Long, S.P., 2003. In vivo temperature response functions of parameters
650   required to model RuBP-limited photosynthesis. Plant Cell Environ. 26 (9), 1419-1430.
651 Bernacchi, C. J., Bagley, J. E., Serbin, S. P., Ruiz-Vera, U. M., Rosenthal, D. M., and Vanloocke, A.2013.
652   Modelling C3 photosynthesis from the chloroplast to the ecosystem, Plant, Cell Environ., 36, 1641-1657,
653   10.1111/pce.12118.
654 Bernacchi, C.J., Singsaas, E.L., Pimentel, C.A.R.L.O.S., Portis Jr., A.R., Long, S.P., 2001. Improved
655   temperature response functions for models of rubisco-limited photosynthesis. Plant Cell Environ. 24 (2),

253-259.

Brunner, M, I., Slater, L., Tallaksen, L, M., Clark M., 2021. Challenges in modeling and predicting floods and droughts: A review. Wiley Interdisciplinary Reviews: Water, 8(3): e1520.

Chen, X., Maignan, F., Viovy, N., Bastos, A., Goll, D., Wu, J., Ciais, P., 2020. Novel representation of leaf phenology improves simulation of Amazonian evergreen forest photosynthesis in a land surface model. Journal of Advances in Modeling Earth Systems, 12(1), e2018MS001565.

Chen, J. M., Ju, W., Ciais, P., Viovy, N., Liu, R., and Liu, Y. 2019.Vegetation structural change since 1981 significantly enhanced the terrestrial carbon sink, Nat. Commun., 10, 4259.

Chen, J. M., Wang, R., Liu, Y., He, L., Croft, H., Luo, X., & Dong, N., 2022. Global datasets of leaf photosynthetic capacity for ecological and earth system research. Earth System Science Data, 14(9), 4077-4093.

Chen, X.*, Ciais, P., Maignan, F., Zhang, Y., Bastos, A., Liu, L., Bacour, C., Fan, L., Gentine, P., Goll, D., Green, J., Kim, H., Li, L., Liu, Y., Peng, S., Tang, H., Viovy, N., Wigneron, J., Wu, J., Yuan, W., Zhang, H. (2021). Vapor pressure deficit and sunlight explain seasonality of leaf phenology and photosynthesis across Amazonian evergreen broadleaved forest. Global Biogeochemical Cycles, 35, e2020GB006893.

Croft, H., Chen, J. M., Wang, R., Mo, G., Luo, S., Luo, X., et al. 2020. The global distribution of leaf chlorophyll content. Remote Sensing of Environment, 236, 111479.

Croft, H., Chen, J. M., Luo, X. Z., Bartlett, P., Chen, B., and Staebler, R. M.: Leaf Chlorophyll Content as a Proxy for Leaf Photosynthetic Capacity, Glob. Change Biol., 23, 3513-3524, https://doi.org/10.1111/gcb.13599, 2017.

Cramer, W., Bondeau, A., Woodward, F. I., Prentice, I. C., Betts, R. A., Brovkin, V., Cox, P. M., Fisher, V., Foley, J. A., Friend, A. D., Kucharik, C., Lomas, M. R., Ramankutty, N., Sitch, S., Smith, B., White, A., and Young-Molling, C. 2001. Global response of terrestrial ecosystem structure and function to CO2 and climate change: results from six dynamic global vegetation models, Glob. Change Biol., 7, 357–373, https://doi.org/10.1046/j.1365-2486.2001.00383.x.

Chou, S., Chen, B., Chen, J., Wang, M., Wang, S., Croft, H., Shi, Q., 2020. Estimation of leaf photosynthetic capacity from the photochemical reflectance index and leaf pigments. Ecol. Indic. 110, 105867.

Crous, K, Y., Uddling, J., De, Kauwe, M, G., 2022. Temperature responses of photosynthesis and respiration in evergreen trees from boreal to tropical latitudes. New Phytologist, 234(2): 353-374.

De chant, B., Cuntz, M., Vohland, M., Schulz, E., & Doktor, D. 2017. Estimation of photosynthesis traits from leaf reflectance spectra: Correlation to nitrogen content as the dominant mechanism. Remote Sensing of Environment, 196, 279–292. RSE.2017.05.019

De chant, B., Ryu, Y., Badgley, G., Zeng, Y., Berry, J. A., Zhang, Y., Goulas, T., Li, Z., Zhang, Q., Kang, M., Li, J., and Moya, I. 2020. Canopy structure explains the relationship between photosynthesis and sun-induced chlorophyll fluorescence in crops, Remote Sens. Environ., 241, 111733.

De Weirdt, M., Verbeeck, H., Maignan, F., Peylin, P., Poulter, B., Bonal, D., et al. 2012. Seasonal leaf dynamics for tropical evergreen forests in a process‐based global ecosystem model. Geoscientific Model Development, 5(5), 1091-1108.

Evans, J. R. (1989). Photosynthesis and nitrogen relationships in leaves of C3 plants. Oecologia, 78(1), 9-19.

Echeverría-Londoño, S., Enquist, B, J., Neves, D, M., Cyrille, V., Brad, B., Nathan, J, B, K., Brian, S, M., Brian, M., Robert, K, P., Brody, S., Stephen, A, S., Jens-Christian, S., Susan, K, W., Andrew, J.K., 2018. Plant functional diversity and the biogeography of biomes in North and South America. Frontiers in Ecology and Evolution, 6: 219.

Fabre, D., Yin, X., Dingkuhn, M., Clément-Vidal, A., Roques, S., Rouan, L., Luquet, D., 2019. Is triose

phosphate utilization involved in the feedback inhibition of photosynthesis in rice under conditions of sink limitation. Journal of Experimental Botany, 70(20), 5773-5785.

Frankenberg, C., Fisher, J. B., Worden, J., Badgley, G., Saatchi, S. S., Lee, J. E., and Kuze, A. 2011. New global observations of the terrestrial carbon cycle from GOSAT: Patterns of plant fluorescence with gross primary productivity, Geophys. Res. Lett., 38, L17706.

Farquhar, G, D., Caemmerer, S, V., Berry, J, A., 1980. A biochemical model of photosynthetic CO_2 assimilation in leaves of C 3 species. planta, 149, 78-90.

Harris, D, N., Adams, S, J., 2007. Understanding the level and causes of teacher turnover: A comparison with other professions. Economics of Education Review, 26(3): 325-337.

Houborg, R., Cescatti, A., Migliavacca, M., & Kustas, W. P. 2013. Satellite retrievals of leaf chlorophyll and photosynthetic capacity for improved modeling of GPP. Agricultural and Forest Meteorology, 177, 10–23

Houborg, R., McCabe, M. F., Cescatti, A., & Gitelson, A. A. 2015. Leaf chlorophyll constraint on model simulated gross primary productivity in agricultural systems. International Journal of Applied Earth Observation and Geoinformation, 43, 160–176.

Hakala, K., Addor, N., Teutschbein, C., Marc, J, P, V., 2019. Hydrological modeling of climate change impacts. Encyclopedia of water: Science, technology, and society, 1-20.

He, L., Chen, J, M., Liu, J., Zheng, T., Wang, R., Joiner, J., Rogers, C., 2019. Diverse photosynthetic capacity of global ecosystems mapped by satellite chlorophyll fluorescence measurements. Remote Sensing of Environment, 232, 111344.

Hikosaka, K. 2014. Optimal nitrogen distribution within a leaf canopy under direct and diffuse light. Plant, Cell & Environment, 37(9), 2077-2085.

Ishida, F. Y., Feldpausch, T. R., Grace, J., Meir, P. W., Saiz, G., Séné, O., Lloyd, J., 2015. Biome-specific effects of nitrogen and phosphorus on the photosynthetic characteristics of trees at a forest-savanna boundary in Cameroon, 178(3): 659-672.

Jensen, A, M., Warren, J, M., Hanson, P, J., Joanne, C., Stan, D, W., 2015. Needle age and season influence photosynthetic temperature response and total annual carbon uptake in mature Picea mariana trees. Annals of Botany, 116(5): 821-832.

Juliane Menezes, Sabrina Garcia, Adriana Grandis, Henrique Nascimento, Tomas F Domingues, Alacimar V Guedes, Izabela Aleixo, Plínio Camargo, Jéssica Campos, Amanda Damasceno, Renann Dias-Silva, Katrin Fleischer, Bart Kruijt, Amanda L Cordeiro, Nathielly P Martins, Patrick Meir, Richard J Norby, Iokanam Pereira, Bruno Portela, Anja Rammig, Ana Gracy Ribeiro, David M Lapola, Carlos A Quesada, 2022. Changes in leaf functional traits with leaf age: when do leaves decrease their photosynthetic capacity in Amazonian trees? Tree Physiology, 42(5), 922-938.

Jung, M., Koirala, S., Weber, U., Ichii, K., Gans, F., Camps-Valls, G., Papale, D., Schwalm, C., Tramontana, G., and Reichstein, M. 2019. The FLUXCOM ensemble of global land-atmosphere energy fluxes, Sci. Data, 6, 7.

Krause, A., Papastefanou, P., Gregor, K., Lucia, S, L., Christian, S, Z.., Allan, B., Xing, L., Jingfeng, X., Anja, R., 2022. Quantifying the impacts of land cover change on gross primary productivity globally. Scientific reports, 12(1): 18398.

Knyazikhin, Y., Schull, M. A., Stenberg, P., Mõttus, M., Rautiainen, M., Yang, Y., et al. 2013. Hyperspectral remote sensing of foliar nitrogen content. Proceedings of the National Academy of Sciences of the United States of America, 110(3), E185-E192.

Kiehn, W, M., 2013. Oligohaline wetland response and recovery following storm-driven saltwater intrusion

744   in coastal Louisiana[M]. Louisiana State University and Agricultural & Mechanical College.

745 Li, X., Du, H., Zhou, G., Mao, F., Zhang, M., Han, N., Mei, T., 2021. Phenology estimation of subtropical
746   bamboo forests based on assimilated MODIS LAI time series data. ISPRS Journal of Photogrammetry
747   and Remote Sensing, 173, 262-277.

748 Lin, Y.-S., Medlyn, B. E., Duursma, R. A., Prentice, I. C., Wang, H., Baig, S., Eamus, D., de Dios, Victor R.,
749   Mitchell, P., Ellsworth, D. S., de Beeck, M. O., Wallin, G., Uddling, J., Tarvainen, L., Linderson, M.-L.,
750   Cernusak, L. A., Nippert, J. B., Ocheltree, T. W., Tissue, D. T., Martin-StPaul, N. K., Rogers, A., Warren,
751   J. M., De Angelis, P., Hikosaka, K., Han, Q., Onoda, Y., Gimeno, T. E., Barton, C. V. M., Bennie, J.,
752   Bonal, D., Bosc, A., Löw, M., Macinins-Ng, C., Rey, A., Rowland, L., Setterfield, S. A., Tausz-Posch,
753   S., Zaragoza-Castells, J., Broadmeadow, M. S. J., Drake, J. E., Freeman, M., Ghannoum, O., Hutley,
754   Lindsay B., Kelly, J. W., Kikuzawa, K., Kolari, P., Koyama, K., Limousin, J.-M., Meir, P., Lola da Costa,
755   A. C., Mikkelsen, T. N., Salinas, N., Sun, W., and Wingate, L. 2015. Optimal stomatal behaviour around
756   the world, Nat. Clim. Change, 5, 459-464, 10.1038/nclimate2550.

757 Lu, X., Ju, W., Li, J., Croft, H., Chen, J. M., Luo, Y., et al. 2020. Maximum carboxylation rate estimation
758   with chlorophyll content as a proxy of rubisco content. Journal of Geophysical Research:
759   Biogeosciences, 125(8), e2020JG005748.

760 Luo, Y., Medlyn, B., Hui, D., Ellsworth, D., Reynolds, J., Katul, G., 2001. Gross primary productivity in
761   duke forest: modeling synthesis of CO2 experiment and eddy–flux data. Ecological Applications, 11(1),
762   239-252.

763 Luo, Y., 2021. Unexplored drivers of plant phenology: beyond climate. Dissertation, Jena, Friedrich-Schiller-
764   Universität Jena.

765 Luo, X., Croft, H., Chen, J. M., He, L., and Keenan, T. F. 2019. Improved estimation of global photosynthesis
766   using information on leaf chlorophyll content, Glob. Change Biol., 25.

767 Liu, Y., Chen, J. M., Xu, M., Wang, R., Fan, W., Li, W., ... & Smith, N. G. 2024. Improved global estimation
768   of seasonal variations in C3 photosynthetic capacity based on eco-evolutionary optimality hypotheses
769   and remote sensing. Remote Sensing of Environment. 313, 114338.

770 Lu, X., Ju, W., Li, J., Croft, H., Chen, J. M., Luo, Y., et al. 2020. Maximum carboxylation rate estimation
771   with chlorophyll content as a proxy of rubisco content. Journal of Geophysical Research:
772   Biogeosciences, 125(8), e2020JG005748.

773 Lu, X., Croft, H., Chen, J, M., Luo, Y., Ju, W., 2022. Estimating photosynthetic capacity from optimized
774   Rubisco–chlorophyll relationships among vegetation types and under global change. Environmental
775   Research Letters, 17(1): 014028.

776 Lu, X., Vitousek, P, M., Mao, Q., Mo, J., 2021. Nitrogen deposition accelerates soil carbon sequestration in
777   tropical forests. Proceedings of the National Academy of Sciences, 118(16): e2020790118.

778 Luo, Y., 2021. Unexplored drivers of plant phenology: beyond climate. Dissertation, Jena, Friedrich-Schiller-
779   Universität Jena.

780 Luo, Y., Medlyn, B., Hui, D., Ellsworth, D., Reynolds, J., Katul, G., 2001. Gross primary productivity in
781   duke forest: modeling synthesis of CO2 experiment and eddy–flux data. Ecological Applications, 11(1),
782   239-252.

783 McClain, A, M., Sharkey, T, D., 2019. Triose phosphate utilization and beyond: from photosynthesis to end
784   product synthesis. Journal of Experimental Botany, 70(6), 1755-1766.

785 Murphy, B, K., 2020. Investigating the Role of Carbon Stress in the Mortality of Tamarack Seedlings Under
786   a Warming Environment. The University of Western Ontario (Canada).

787 Menezes, J., Garcia, S., Grandis, A., Henrique, N., Tomas, F, D., Alacimar, V, G., Izabela, A., Plínio, C.,

788   Jéssica, C., Amanda, D., Renann, D., Katrin, F., Bart, K., Amanda, L, C., Nathielly, P, M., Patrick, M.,
789   Richard, J, N., Iokanam, P., Bruno, P., Anja, R., Ana, G, R., David, M, L., Carlos, A, Q., 2022. Changes
790   in leaf functional traits with leaf age: when do leaves decrease their photosynthetic capacity in
791   Amazonian trees. Tree physiology, 42(5): 922-938.
792   Medlyn, B. E., Duursma, R. A., Eamus, D., Ellsworth, D. S., Prentice, I. C., Barton, C. V. M., Crous, K. Y.,
793   De Angelis, P., Freeman, M., and Wingate, L. 2011. Reconciling the optimal and empirical approaches
794   to modelling stomatal conductance, Glob. Change Biol., 17, 2134-2144, 10.1111/j.1365-
795   2486.2010.02375.x.
796   Mohammed, G. H., Colombo, R., Middleton, E. M., Rascher, U., van der Tol, C., Nedbal, L., Goulas, Y.,
797   Pérez-Priego, O., Damm, A., Meroni, M., Joiner, J., Cogliati, S., Verhoef, W., Malenovský, Z., Gastellu-
798   Etchegorry, J.-P., Miller, J. R., Guanter, L., Moreno, J., Moya, I., Berry, J. A., Frankenberg, C., and
799   Zarco-Tejada, P. J. 2019. Remote sensing of solar-induced chlorophyll fluorescence (SIF) in vegetation:
800   50 years of progress, Remote Sens. Environ., 231, 111177.
801   Oliveira, F, M, P., Knoechelmann, C, M., Wirth, R., M, T., Inara, R, L., 2023. Leaf‐cutting ant nests support
802   less dense and impoverished seed assemblages in a human‐modified Caatinga dry forest. Biotropica,
803   55(2): 444-453.
804   Onoda, Y., Wright, I. J., Evans, J. R., Hikosaka, K., Kitajima, K., Niinemets, Ü., et al. 2017. Physiological
805   and structural tradeoffs underlying the leaf economics spectrum. New Phytologist, 214(4), 1447-1463.
806   Orndahl, K, M., Ehlers, L, P, W., Herriges, J, D., Rachel, E, P., Mark, H., Scott, J, Goetz., 2022. Map tundra
807   ecosystem plant functional type cover, height, and aboveground biomass in Alaska and northwest
808   Canada using unmanned aerial vehicles. Arctic science, 8(4): 1165-1180.
809   Piao, S., Liu, Q., Chen, A., Janssens, I, A., Fu, Y., Dai, J., Liu, L., Lian, X., Shen, M., Zhu, X., 2019. Plant
810   phenology and global climate change: Current progresses and challenges. Global change biology, 25(6):
811   1922-1940.
812   Pinheiro, Eldestein, C., 2023. Effect of functional diversity on ecosystem services in cocoa agroforestry
813   systems. Maestría en Agroforestería y Agricultura Sostenible.
814   Quebbeman, J. A., & Ramirez, J. A. 2016. Optimal allocation of leaf‐level nitrogen: Implications for
815   covariation of Vcmax and Jmax and photosynthetic downregulation. Journal of Geophysical Research,
816   Biogeosciences, 121(9), 2464-2475.
817   Ryu, Y., Jiang, C., Kobayashi, H., and Detto, M. 2018. MODIS-derived global land products of shortwave
818   radiation and diffuse and total photosynthetically active radiation at 5 km resolution from 2000, Remote
819   Sens. Environ., 204, 812-825, 10.1016/j.rse.2017.09.021.
820   Sharma, U., Kataria, V., Shekhawat, N, S., 2017. In vitro propagation, ex vitro rooting and leaf
821   micromorphology of Bauhinia racemosa Lam.: a leguminous tree with medicinal values. Physiology
822   and Molecular Biology of Plants, 23: 969-977.
823   Sun, J., Sun, J., Feng, Z., 2015. Modelling photosynthesis in flag leaves of winter wheat (Triticum aestivum)
824   considering the variation in photosynthesis parameters during development. Functional Plant Biology,
825   42(11): 1036-1044.
826   Sulla-Menashe, D., Woodcock, C. E., and Friedl, M. A. 2018. Canadian boreal forest greening and browning
827   trends: An analysis of biogeographic patterns and the relative roles of disturbance versus climate drivers,
828   Environ. Res. Lett., 13, 014007.
829   Sulc, R, M., Barker, D, J., Tilmon, K., 2017. Forage production. Ohio Agronomy Guide. Columbus, OH:
830   Ohio State University Extension Bulletin, 472(155): 82-109.
831   Song, G., Wang, Q., 2020. Leaf photosynthetic capacity of sunlit and shaded mature leaves in a deciduous

832   forest. Forests, 11(3): 318.

833   Stocker, B, D., Wang, H., Smith, N, G., 2020. An optimality-based light use efficiency model for simulating
834   ecosystem gross. Geoscientific Model Development, 13 (3).

835   Spafford, L., 2023. Refining terrestrial biosphere feedbacks to climate change through precise
836   characterization of terrestrial vegetation. Memorial University of Newfoundland.

837   Spicer, M, E., Radhamoni, H, V, N., Duguid, M, C., Simon, A, Q., Liza, S, Comita., 2022. Herbaceous plant
838   diversity in forest ecosystems: patterns, mechanisms, and threats. Plant Ecology, 223(2): 117-129.

839   Stefanski, A., Bermudez, R., Sendall, K, M., Montgomery, R, A., Reich, P, B., 2020. Surprising lack of
840   sensitivity of biochemical limitation of photosynthesis of nine tree species to open‐air experimental
841   warming and reduced rainfall in a southern boreal forest. Global change biology, 26(2): 746-759.

842   Urban, O., Šprtová, M., Košvancová, M., Tomášková, I., Lichtenthaler, H, K., Marek, M, V., 2008.
843   Comparison of photosynthetic induction and transient limitations during the induction phase in young
844   and mature leaves from three poplar clones. Tree Physiology, 28(8), 1189-1197.

845   Verheijen, L. M., Brovkin, V., Aerts, R., Bönisch, G., Cornelissen, J. H. C., Kattge, J., et al. 2013. Climate of
846   the past geoscientific instrumentation methods and data systems impacts of trait variation through
847   observed trait‐climate relationships on performance of an Earth system model: A conceptual analysis.
848   Biogeosciences, 10(8), 5497-5515.

849   Walther, S., 2019. Assessment of the dynamics of terrestrial vegetation using satellite observations of
850   greenness and sun-induced chlorophyll fluorescence.

851   Wang, S., Li, Y., Ju, W., Chen, B., Chen, J., Croft H., Mickler, R, A., Yang, F., 2020. Estimation of leaf
852   photosynthetic capacity from leaf chlorophyll content and leaf age in a subtropical evergreen coniferous
853   plantation. Journal of geophysical research: Biogeosciences, 125(2): e2019JG005020.

854   Wang, X., Chen, J. M., Ju, W., Zhang, Y., 2022. Seasonal variations in leaf maximum photosynthetic capacity
855   and its dependence on climate factors across global FLUXNET sites. Journal of Geophysical Research:
856   Biogeosciences, 127(5): e2021JG006709.

857   Wang, Z., 2021. The influences of phosphorus cycling on the tropical ecosystem carbon cycle-A process-
858   based modeling study. Auburn University.

859   Weiss, A. and Norman, J. M.1985. Partitioning solar radiation into direct and diffuse, visible and near-infrared
860   components, Agr. Forest Meteorol., 34, 205-213, 10.1016/0168- 1923(85)90020-6.

861   Wu, J., Kobayashi, H., Stark, S, C., Meng, R., Guan, K., Tran, N, N., Saleska, S, R., 2018. Biological
862   processes dominate seasonality of remotely sensed canopy greenness in an Amazon evergreen
863   forest. New Phytologist, 217(4), 1507-1520.

864   Wu, J., Guan, K., Hayek, M., Restrepo-Coupe, N., Wiedemann, K. T., Xu, X., et al. 2017. Partitioning
865   controls on Amazon forest photosynthesis between environmental and biotic factors at hourly to
866   interannual timescales. Global Change Biology, 23(3), 1240-1257.

867   Wu, J., Albert, L. P., Lopes, A. P., Restrepo-Coupe, N., Hayek, M., Wiedemann, K. T., et al. 2016. Leaf
868   development and demography explain photosynthetic seasonality in Amazon evergreen forests. Science,
869   351(6276), 972-976.

870   Xu, M., Liu, R., Chen, J.M., Liu, Y., Wolanin, A., Croft, H., et al., 2022a. A 21-year time series of global leaf
871   chlorophyll content maps from MODIS imagery. IEEE Trans. Geosci. Remote Sens. 60, 1–13.

872   Xu, M., Liu, R., Chen, J.M., Shang, R., Liu, Y., Qi, L., et al., 2022b. Retrieving global leaf chlorophyll content
873   from MERIS data using a neural network method. ISPRS Journal of Photogrammetry and Remote
874   Sensing 192, 66-82.

875   Xu, X., Medvigy, D., Joseph, W. S., Kitajima, K., Wu, J., Albert, L. P., et al. 2017. Variations of leaf longevity

876   in tropical moist forests predicted by a trait-driven carbon optimality model. Ecology letters, 20(9),
877   1097–1106.
878 Yang, J, T., Preiser, A, L., Li, Z., Weise, S, E., Sharkey, T, D., 2016. Triose phosphate use limitation of
879   photosynthesis: short-term and long-term effects. Planta, 243, 687-698.
880 Yang, X., Wu, J., Chen,X.*, Ciais, P., Maignan, F., Yuan, W., Piao, S., Yang, S., Gong, F., Su, Y., Dai, Y., Liu,
881   L., Zhang, H., Bonal, D., Liu, H., Chen, G., Lu, H., Wu, S., Fan, L., Gentine, P., Wright, S. J. (2021). A
882   comprehensive framework for seasonal controls of leaf abscission and productivity in evergreen,
883   broadleaved tropical and subtropical forests. The Innovation, 2(4), 100154.
884 Yang, X., Wu, J., Chen, X., Ciais, P., Maignan, F., Yuan, W., Piao, S., Yang, S., Gong, F., Su, Y., Dai, Y., Liu,
885   L., Zhang, H., Bonal, D., Liu, H., Chen, G., Lu, H., Wu, S., Fan, L., Gentine, P., and Wright, S. J. 2021
886   A comprehensive framework for seasonal controls of leaf abscission and productivity in evergreen
887   broadleaved tropical and subtropical forests, Innovation, 2, 100154.
888 Yang, X., Tang, J., Mustard, J. F., Lee, J.-E., Rossini, M., Joiner, J., Munger, J. W., Kornfeld, A., and
889   Richardson, A. D. 2015. Solarinduced chlorophyll fluorescence that correlates with canopy
890   photosynthesis on diurnal and seasonal scales in a temperate deciduous forest, Geophys. Res. Lett., 42,
891   2977–2987.
892 Yang, X., Chen, X., Ren, J., Yuan, W., Liu, L., Liu, J., Chen, D., Xiao, Y., Song, Q., Du, Y., Wu, S., Fan, L.,
893   Dai, X., Wang, Y., Su, Y., 2023. A gridded dataset of a leaf-age-dependent leaf area index seasonality
894   product over tropical and subtropical evergreen broadleaved forests. Earth System Science Data, 15(6):
895   2601-2622.
896 Yang, X., Sun, Q., Han, L., and Chen, X. 2025. A gridded dataset of young leaf photosynthetic capacity
897   product over tropical and subtropical evergreen broadleaved forests [Data set]. Zenodo.
898   https://doi.org/10.5281/zenodo.14807414
899 Zhao, B., 2019. Comparing Autumn Phenology Derived from Field Observations, Satellite Data, and Carbon
900   Flux Measurements in a Northern Mixed Forest.
901 Zhao, Y., Chen, X., Smallman, T. L., Flack-Prain, S., Milodowski, D. T., and Williams, M.: Characterizing
902   the Error and Bias of Remotely Sensed LAI Products: An Example for Tropical and Subtropical
903   Evergreen Forests in South China, Remote Sens., 12, 3122, 10.3390/rs12193122, 2020.
904 Zhou, H., Xu, M., Pan, H., Yu, X., 2015. Leaf-age effects on temperature responses of photosynthesis and
905   respiration of an alpine oak, Quercus aquifolioides, in southwestern China. Tree physiology, 35(11),
906   1236-1248.
907 Locke A.M., Ort D.R., 2014. Leaf hydraulic conductance declines in coordination with photosynthesis,
908   transpiration and leaf water status as soybean leaves age regardless of soil moisture. J Exp Bot. 65,
909   6617-6627.
910